The ocean mixed layer under Southern Ocean sea-ice: Seasonal cycle and forcing

Violaine Pellichero, Jean-Baptiste Sallée, Sunke Schmidtko, Fabien Roquet, Jean-Benoit Charrassin

AGU PUBLICATIONS

JGR

Journal of Geophysical Research: Oceans

RESEARCH ARTICLE

10.1002/2016JC011970

The ocean mixed layer under Southern Ocean sea-ice: Seasonal cycle and forcing

Violaine Pellichero [1], Jean-Baptiste Sallée [1], Sunke Schmidtko [2], Fabien Roquet [3], and Jean-Benoît Charrassin [1]

[1]Sorbonne Universités, UPMC Univ., Paris 06, UMR 7159, LOCEAN-IPSL F-75005, Paris, France, [2]GEOMAR Helmholtz Centre for Ocean Research Kiel, Kiel, Germany, [3]Department of Meteorology, Stockholm University, Stockholm, Sweden

Key Points:
- Climatological seasonal cycle of under-ice mixed layer in the Southern Ocean is produced with unprecented number of observations
- Under-ice seasonal cycle of mixed-layer buoyancy content and stability is primarily driven by their haline contributions
- Buoyancy content of under-ice mixed layer is predominantly explained by ice-ocean and vertical entrainment fluxes

Correspondence to:
V. Pellichero,
violaine.pellichero@locean-ipsl.upmc.fr

Citation:
Pellichero, V., J.-B. Sallée, S. Schmidtko, F. Roquet, and J.-B. Charrassin (2017), The ocean mixed layer under Southern Ocean sea-ice: Seasonal cycle and forcing, *J. Geophys. Res. Oceans*, *122*, 1608–1633, doi:10.1002/2016JC011970.

Received 18 MAY 2016
Accepted 21 NOV 2016
Accepted article online 28 NOV 2016
Published online 27 FEB 2017

Abstract The oceanic mixed layer is the gateway for the exchanges between the atmosphere and the ocean; in this layer, all hydrographic ocean properties are set for months to millennia. A vast area of the Southern Ocean is seasonally capped by sea-ice, which alters the characteristics of the ocean mixed layer. The interaction between the ocean mixed layer and sea-ice plays a key role for water mass transformation, the carbon cycle, sea-ice dynamics, and ultimately for the climate as a whole. However, the structure and characteristics of the under-ice mixed layer are poorly understood due to the sparseness of in situ observations and measurements. In this study, we combine distinct sources of observations to overcome this lack in our understanding of the polar regions. Working with elephant seal-derived, ship-based, and Argo float observations, we describe the seasonal cycle of the ocean mixed-layer characteristics and stability of the ocean mixed layer over the Southern Ocean and specifically under sea-ice. Mixed-layer heat and freshwater budgets are used to investigate the main forcing mechanisms of the mixed-layer seasonal cycle. The seasonal variability of sea surface salinity and temperature are primarily driven by surface processes, dominated by sea-ice freshwater flux for the salt budget and by air-sea flux for the heat budget. Ekman advection, vertical diffusivity, and vertical entrainment play only secondary roles. Our results suggest that changes in regional sea-ice distribution and annual duration, as currently observed, widely affect the buoyancy budget of the underlying mixed layer, and impact large-scale water mass formation and transformation with far reaching consequences for ocean ventilation.

1. Introduction

The surface of the ocean is mixed by wind-induced turbulence and buoyancy fluxes at the air-sea interface. This mixing maintains a neutrally buoyant and vertically uniform layer at the surface of the World's ocean, commonly referred to as the ocean mixed layer. The mixed layer acts as a barrier and bridge between the atmosphere and the ocean interior [*de Boyer Montégut et al*., 2004; *Holte and Talley*, 2009], and modulates all exchanges between air and sea (dynamic exchanges, thermodynamics exchanges, or biogeochemical exchanges). For instance, the characteristics of the ocean mixed layer largely determine the distribution and properties of the World's ocean water masses [*Sprintall and Roemmich*, 1999; *de Boyer Montégut et al*., 2004] and govern the ocean capacity to store heat and carbon [*Sallée et al*., 2012; *Lévy et al*., 2015]. In the Southern Ocean, the mixed layer plays an outsized role as it allows world deep waters to ventilate and to acquire their characteristics [*Rintoul et al*., 2001]. A large fraction of the interior ocean water masses have had their last contact with the atmosphere in the Southern Ocean mixed layers (more than half of the global ocean volume according to *DeVries and Primeau* [2011]). This central role played by the Southern Ocean is associated with a large water mass overturning [*Iudicone et al*., 2008; *de Lavergne et al*., 2015]. In the Southern Overturning circulation, deep waters upwell toward the ocean surface, where water masses are transformed in the mixed layer, and are reinjected back in deeper or shallower layers [*Whitworth et al*., 1998]. Therefore, a majority of the World's ocean acquires its physical and biogeochemical characteristics in the Southern Ocean mixed layer before being isolated from the atmosphere for millennia (the mean ventilation age is ~300–1500 years according to *DeVries and Primeau* [2011]).

The Southern Ocean overturning circulation interacts with the intense eddy-dominated circulation of the Antarctic Circumpolar Current (ACC), with a mean westward flow in the latitudinal range 50°S–60°S. Over

the last couple of decades within and north of the ACC, the Southern Ocean mixed layer has been extensively observed by international programs such as WOCE, CLIVAR, GO-SHIP, or Argo. A number of studies describe a very marked seasonal cycle of the ocean surface layer, with deep destabilization of the mixed layer in winter, primarily caused by air-sea fluxes, Ekman heat transport, and vertical entrainment [e.g., *Sallée et al*., 2006; *Dong et al*., 2007, 2008; *Ren et al*., 2011]. In contrast, observational data in region south of the ACC, characterized by subpolar gyre circulation systems and by a seasonal sea-ice cap, are much sparser. The paucity of ocean observations is primarily due to the difficulty of winter access to these regions and results in our lack of knowledge and understanding of local processes. The presence of sea-ice makes ship-based observation complex, prevents satellite communication with autonomous platforms, and limits large-scale satellite-based observation of the ocean surface. The seasonal cycle of the mixed layer in the subpolar gyre sectors of the Southern Ocean is thought to be strongly influenced by seasonal varying ocean-ice freshwater fluxes with summer sea-ice melt associated with a net freshening and lightening of the mixed layer, and winter sea-ice formation associated with a net densification and deepening of the mixed layer [*Ren et al*., 2011; *Petty et al*., 2014; *Barthélemy et al*., 2015]. This seasonal cycle can be associated with major water mass transformation along the Antarctic coast and in the subpolar gyres [*Whitworth et al*., 1998; *Talley et al*., 2007; *Tamura et al*., 2011]. This region is central for the dynamics of the Southern Ocean, with most of the Southern Ocean dense water upwelling occurring south of the ACC [*Rintoul et al*., 2001].

With this study, we want to shed light on the seasonal cycle of the mixed layer in the regions south of the ACC, seasonally capped by sea-ice, by exploiting more than 10 years of observations from instrumentation of southern elephant seals with satellite-linked Conductivity-Temperature-Depth sensors collected as part of several marine ecology research programs [*Biuw et al*., 2007; *Charrassin et al*., 2008; *Roquet et al*., 2013, 2014]. Elephant seals spend a significant part of their annual life cycle south of 60°S and dive routinely to depth exceeding 500 m. Therefore, this data set significantly increases the temporal and spatial coverage of ocean observations in the Antarctic sea-ice, as well as on the Antarctic continental slope and shelf regions, which are outside the conventional areas of Argo autonomous floats and ship-based studies. Using the combination of elephant seal-derived, Argo, and ship-based observations, we describe the seasonal cycle of the characteristics and stability of the ocean mixed layer over the entire Southern Ocean (south of 30°S). In particular, we use an unprecedented number of ocean observations, including more than 100,000 profiles in the seasonally capped sea-ice sector. To this end, we first construct a robust climatology of mixed-layer characteristics over the entire Southern Ocean up to the Antarctic continental shelves. We then investigate how the stratification at the base of the mixed layer is seasonally eroded and reformed by a combination of ocean processes and ocean-ice-atmosphere processes.

This study is laid out as follows: our data, the protocol to estimate the mixed-layer characteristics, and the governing equation for its density, salinity, and temperature balance are introduced in section 2. The results are presented in section 3 and discussed in section 4. Finally, section 5 contains a condensed summary.

2. Materials and Methods

2.1. Data

In this study, we employ three distinct sources of observations to maximize the number of profiles in the Southern Ocean, where historically the observations are sparse.

The first set of observations contains conductivity-temperature-depth (CTD) data from ship-recorded observations during the period 1906–2012 from the NOAA World Ocean Database (https://www.nodc.noaa.gov/OC5/SELECT/dbsearch/dbsearch.html). We only use profiles that have a quality control flag of 1, containing information on their position, date, temperature, and salinity profiles. This hydrographic data set is augmented by float data from the Argo international program. The Argo program started in 2000 and has critically increased the number of ocean observations sampled every year over the World oceans [*Riser et al*., 2016]. The Argo float profiles of pressure, salinity, and temperature used in this study were gathered in the period 2002–2014. They provide temperature and salinity between 0 and 2000 m at an accuracy of ± 0.005°C and ± 0.01 PSU, respectively. We only use profiles that have a quality control flag of 1, and contain information on their position, date, temperature, and salinity profiles. As a final data set, we use profiles derived from the animal-borne sensor programs [*Charrassin et al*., 2008; *Roquet et al*., 2013], i.e., southern elephant seals equipped with satellite-linked CTD sensors. Since 2004, the

instrumentation of southern elephant seals with CTD unit has provided unique spatial and temporal coverage of the southernmost part of the Southern Ocean. We use a calibrated data set from *Roquet et al*. [2014]. Once calibrated, the accuracy of the data is estimated to be ±0.03°C in temperature and ±0.05 in salinity. Under optimum conditions, these accuracies may reach ±0.01°C and ±0.02, respectively. The effect of these instrumental errors is propagated through all our calculations to investigate impact on our results (see Appendix A).

One important characteristic of these three sources of observations is that they are spatially and temporally complementary. Ship-based observations are carried out mostly during summer because of the extreme climate conditions in winter, and they concentrate near the coasts (Figures 1a and 1e). In contrast, Argo float observations fill the middle of the ocean basins, and cover the entire seasonal cycle, but leave out the entire region seasonally capped by sea-ice (except selected floats in the Weddell Sea region where under-ice Argo network has been growing over the last years; Figures 1b and 1e) [*Reeve et al*., 2015]. The instrumented seals data set covers the entire region south of the ACC fronts, and provides observations over the entire seasonal cycle (Figures 1c and 1e). Overall, the combination of these three data sets provides us with an unprecedented cover of the Southern Ocean over the entire seasonal cycle (Figures 1d and 1e). We note however that the Ross Sea sector is the least well-covered region. Therefore, our results as presented below might not represent the state of the Ross Sea as accurately as the rest of Antarctica.

The combination of the three data sets is however heterogeneous in terms of vertical resolution of the hydrographic profiles they provide: if ship-based profiles have resolution of the order of 1 dbar, most Argo profiles have a resolution of the order of 10 dbar, and instrumented seals profiles have a resolution of a few tens of dbar (typically 15 points per profile automatically selected before being sent by satellite based on the shape of the temperature/salinity profiles) [*Roquet et al*., 2014]. Our mixed-layer detection procedure must therefore be robust enough to perform well with this variety of profile resolutions. We described our methods for a robust mixed-layer determination in the following section.

2.2. Estimation of the Mixed-Layer Depth

The properties and vertical extent of the mixed layer are the most important factors for most physical and biological ocean surface processes. The mixed layer is defined as the surface ocean slab where physical properties such as density, salinity, or temperature are well mixed, i.e., nearly homogeneous with depth. A number of methods have been developed over the years to compute mixed-layer depth based on a given density, salinity, or temperature profile [e.g., *Brainerd and Gregg*, 1995; *Thomson and Fine*, 2003; *de Boyer Montégut et al*., 2004; *Holte and Talley*, 2009].

It has been shown that methods working on density profiles rather than temperature profiles are more successful in detecting the base of the mixed layer in the Southern Ocean [e.g., *Lukas and Lindstrom*, 1991; *Sallée et al*., 2006; *Holte and Talley*, 2009]. We therefore chose to work on the density profile and use a hybrid method analyzing the general shape of each profile, searching for physical features in the profile, and calculating a density threshold and vertical density gradient to assemble a suite of possible mixed-layer depth values [*Holte and Talley*, 2009]. The method therefore produces three estimates of mixed-layer depth (MLD): MLD_{shape}, $MLD_{threshold}$, and $MLD_{gradient}$, and an algorithm then computes the most plausible mixed-layer depth value as a combination of these three estimates, MLD_{Holte} (see *Holte and Talley* [2009] for more details). Figure 2 provides an example of two typical instrumented seal profiles and associated suite of mixed-layer depth estimates.

As described above, our data set is heterogeneous in terms of vertical resolution, and specifically includes profiles from instrumented seals with a relatively low vertical resolution, which can cause some issues in the detection of a mixed-layer base compared to working on higher-resolution profiles. In order to reduce the risk of systematic bias in our mixed-layer detection, we eye-checked a high number of profiles. As part of this procedure, it appeared that MLD_{Holte} was for many profiles slightly more accurate than $MLD_{gradient}$, $MLD_{threshold}$, or MLD_{shape}, but that for other profiles (complex shaped profiles due to low resolution), MLD_{Holte} was considered misplaced to what we would have said by eye. We therefore chose to always trust MLD_{Holte} as a reliable estimate of the mixed-layer depth (h_m), but add a constraint to this choice, to make sure h_m also "somewhat agrees" with at least two of the more widely used methods ($MLD_{gradient}$, $MLD_{threshold}$ or MLD_{shape}), as follows:

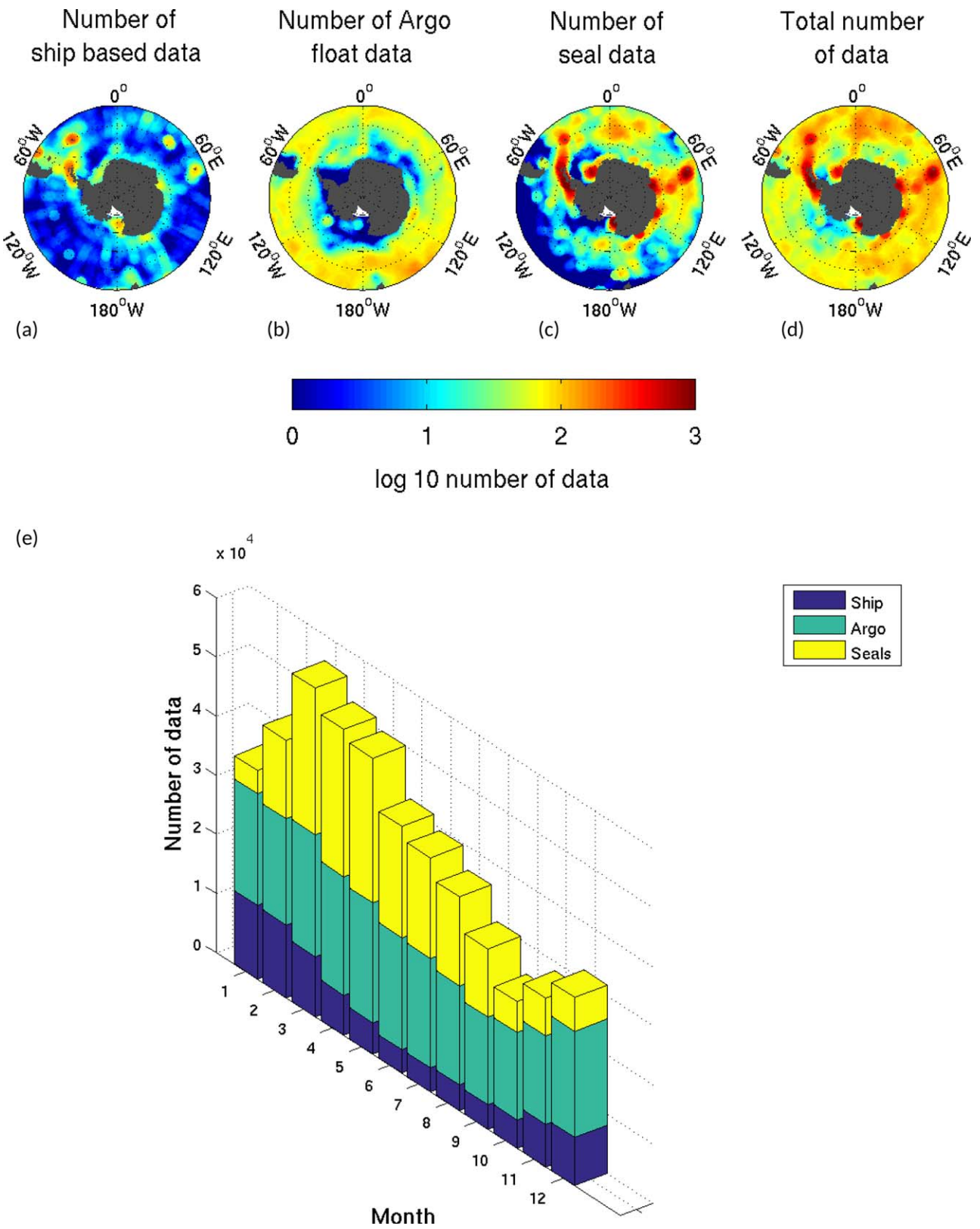

Figure 1. Spatial distribution within mapping radius of the grid used of (d) the total number of data and according subsets: (a) ship-based data, (b) Argo float data, and (c) elephant seals data. (e) Monthly evolution of the number of data for each data set.

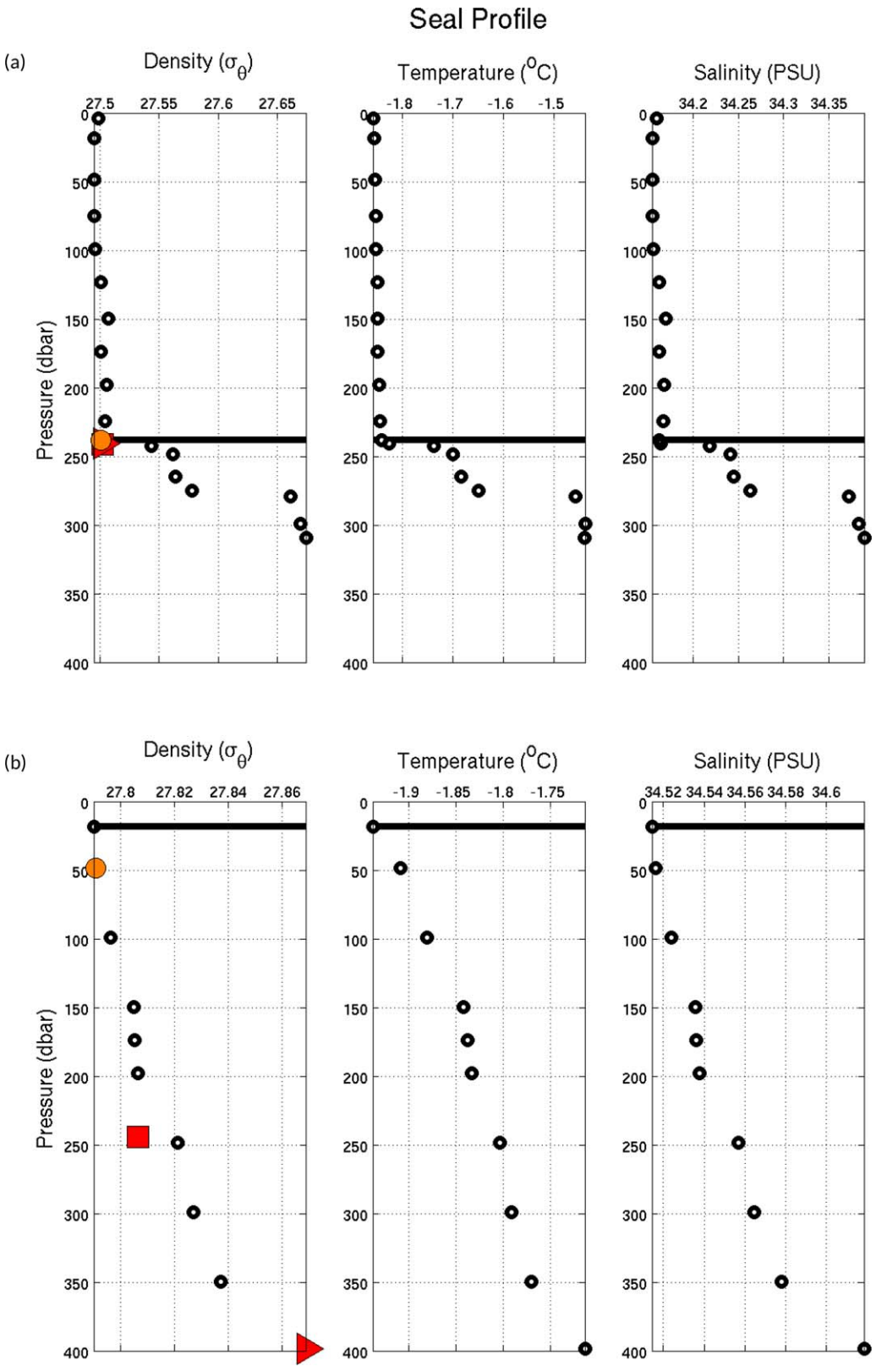

Figure 2. Two selected potential density, temperature, and salinity profiles (black dots) from an elephant seal as well as the four MLD estimates from the density threshold method (red square), density gradient method (red triangle), fitting method (orange circle), and the Holte and Talley's algorithm (horizontal solid line). (top) A profile where the four methods are in agreement, and (bottom) a profile where the four methods disagree and thus we reject the profile of our climatology.

$$h_m = \begin{cases} MLD_{Holte}, & \text{if } \sigma(\mathrm{MLD}_{Holte}, \mathrm{MLD}_{threshold}, \mathrm{MLD}_{gradient}) \leq 1/4\mathrm{MLD}_{Holte} \\ MLD_{Holte}, & \text{if } \sigma(\mathrm{MLD}_{Holte}, \mathrm{MLD}_{shape}, \mathrm{MLD}_{gradient}) \leq 1/4\mathrm{MLD}_{Holte} \\ MLD_{Holte}, & \text{if } \sigma(\mathrm{MLD}_{Holte}, \mathrm{MLD}_{threshold}, \mathrm{MLD}_{shape}) \leq 1/4\mathrm{MLD}_{Holte} \\ Undefined, & \text{otherwise.} \end{cases} \quad (1)$$

In some cases, MLD_{Holte} is equal to either MLD_{shape}, $\mathrm{MLD}_{gradient}$ or $\mathrm{MLD}_{threshold}$ (by construction; see *Holte and Talley* [2009]), so the standard deviation is most likely small. In some other cases, MLD_{Holte} is neither equal to MLD_{shape}, $\mathrm{MLD}_{gradient}$ nor $\mathrm{MLD}_{threshold}$. The standard deviation criteria allow to keep the value when it is not too dissimilar than the more commonly used methods (MLD_{shape}, $\mathrm{MLD}_{gradient}$ or $\mathrm{MLD}_{threshold}$), and reject it when the value is very different. This procedure rejects about 20% of profiles of our total database but gives us confidence that our computed mixed layer is robust, without having to eye-check the 600,000 profiles from our database. Selected visual inspection was performed on a series of profiles to ensure the quality of the computed mixed-layer depth (see two examples in Figure 2). Error associated to this mixed-layer detection procedure is discussed in Appendix A.

2.3. Mixed-Layer Properties and Static Stability at the Base of the Mixed Layer

For each profile that was not rejected in the process of determining the mixed layer, we compute a number of properties of the mixed layer: mean conservative temperature (T_m), mean absolute salinity (S_m), mean potential density as well as the vertical stability at the base of the mixed layer [*IOC et al.*, 2010; *Roquet et al.*, 2015]. The vertical stability of a water column is given by the Brunt-*Väisälä* coefficient:

$$N^2 = -\frac{g}{\rho} \times \frac{\partial \sigma_o}{\partial z}, \quad (2)$$

where g is the gravity acceleration, ρ is the in situ density, and σ_o the surface-referenced potential density. N^2 is computed over a constant depth range of 15 m, directly below the mixed-layer base.

The water column is stable only if N^2 is positive. The smaller is N^2, the less energy is required to mix the water column [*Gill*, 1982]. The Brunt-*Väisälä* coefficient is therefore a useful indication of the preconditioning of the base of the mixed layer for further deepening. This stability of the water column can be expressed by a linear combination of the stability of the temperature profile and the stability of the salinity profile [*Gill*, 1982]:

$$N^2 = N_T^2 + N_S^2, \quad (3)$$

$$N_S^2 = -g\beta \frac{\partial S_m}{\partial z}, \quad (4)$$

$$N_T^2 = g\alpha \frac{\partial T_m}{\partial z}, \quad (5)$$

where β is the saline contraction coefficient at constant pressure defined as $\beta = (1/\rho) \times \partial\rho/\partial S$ and α is the thermal expansion coefficient at constant pressure defined as $\alpha = -(1/\rho) \times \partial\rho/\partial T$.

2.4. Optimal Interpolation

Once the depth and various properties of the mixed layer have been computed for all individual profiles, we produced monthly climatological fields of each of these quantities using an Optimal Interpolation procedure. The Optimal Interpolation and gridding method is described in detail in *Schmidtko et al.* [2013]. As a brief summary, we interpolate onto a half degree grid from the South Pole to 30°S, and over the entire circumpolar belt. We used a 550 km isotropic decorrelation scale, but incorporating an anisotropic isobath-following component using a "Fast Marching" algorithm, as well as front-sharpening components. In addition, recent data are emphasized in the mapping, which produces a climatology typical of the years 2000–2010 (see *Schmidtko et al.* [2013] for more details on the mapping).

Errors associated with the interpolated fields have been computed by propagating a number of individual sources of uncertainty into our interpolation procedure: e.g., instrumental errors and how they translate into MLD, and associated mixed-layer temperature and salinity, or decorrelation scale (see Appendix A). Regions that exhibit largest errors are located around the Antarctic coast, within the ACC and directly north

of it, presumably because they are regions with weak stratification, i.e., where small errors translate into large deviation of the mixed-layer base and associated characteristics. Our mean climatological maps are, however, somewhat stable, with errors on MLD of only several tens of meters in the weakly stratified regions. Within the sea-ice sector, regional variability of temperature is very weak, with temperature being highly constraint by freezing point, hence the interpolation error is small for temperature in sea-ice zone. In contrast, salinity errors have more regional structure, probably due to data availability and quality of sensors. All details and seasonal error maps are given in Appendix A.

2.5. Sea-Ice Extent

This paper focuses on mixed-layer properties and budget over the Southern Ocean. One key aspect of the Southern Ocean is the seasonal sea-ice cap, and we therefore often refer in the text to "sea-ice sector" or "ice-free sector." Unless otherwise noted, "sea-ice sector" corresponds to the area defined by the winter maximum of sea-ice cover (fixed in September), with a sea-ice concentration greater than 15% [e.g., *Zwally et al*., 2002]. However, fixing the sea-ice sector as the September, 15% concentration maximum may lead to miss-representing the mixed-layer properties since some observations within the sea-ice zone could likely come from observations in open water near the ice, rather than actually under sea-ice. To test the relevance of our choice for the sea-ice sector, we collocated all individual profiles used in our analysis with instantaneous sea-ice concentration, available from 1980 to now. This way we can distinguish the profiles which are actually sampled in the sea-ice covered region, and those which are not. We then performed the exact same interpolation procedure as presented in this paper, but only with these profiles. The resulting climatological fields are both qualitatively and quantitatively, the same than those described in the present study.

We use satellite-derived observations of sea-ice concentration from Nimbus-7 SMMR and DMSP SSM/I-SSMIS passive microwave data at a daily and 25 km resolution [*Cavalieri et al*., 1997]. From this data set, we produce a climatological sea-ice concentration seasonal cycle for the decade 2000–2010 (to match the typical time period of our ocean observations) from which we compute the sea-ice extent.

2.6. Mixed-Layer Salinity and Temperature Budget

We investigate the processes controlling the variability of the mixed-layer salinity (S_m) and temperature (T_m). As such we derived the salt and temperature balance equations, describing the rate of change of salinity and temperature in terms of diffusive processes, horizontal advective fluxes (geostrophic and ageostrophic including Ekman), vertical entrainment at the base of the mixed layer, and air-ice-sea fluxes [e.g., *Dong et al*., 2007; *Ren et al*., 2011]:

$$\frac{\partial S_m}{\partial t} = \frac{S_m FWF}{h_m} - u_m.\nabla S_m + \kappa \frac{\partial S_m}{\partial z} - \frac{w_e \Delta S_m}{h_m}, \tag{6}$$

$$\frac{\partial T_m}{\partial t} = \frac{Q_{net}}{\rho_0 C_p h_m} - u_m.\nabla T_m + \kappa \frac{\partial T_m}{\partial z} - \frac{w_e \Delta T_m}{h_m}, \tag{7}$$

where C_p is the specific heat of sea water, Q_{net} is the total heat flux into the mixed layer, *FWF* represents the net air-ice-sea freshwater flux from evaporation, precipitation, and ice formation/melt, u_m is the horizontal velocity, κ is the vertical turbulent diffusion coefficient at the base of the mixed layer, ΔS_m and ΔT_m correspond to the salinity and temperature differences at the base of the mixed layer, and w_e is the entrainment velocity.

In the following, we consider that the horizontal velocity is solely the Ekman flow (see section 2.7). It is important to note that this is certainly a strongly simplified assumption, as geostrophic velocity is undoubtedly an important, if not dominant, contribution to the horizontal velocity. However, in this study, we perform a circumpolar integrated budget, and given that the geostrophic velocity is predominantly zonal, the geostrophic flow in and out of our circumpolar domain is small. In order to test this assumption, we estimated the mean geostrophic flow under sea-ice from a mean dynamic topography at ocean surface provided by AVISO [*Rio et al*., 2014]. Much care must be taken when working with such product in sea-ice zone, as they are only weakly constrained by observations. Estimating the mean geostrophic heat and freshwater transports with this product, we find they are negligible (order of magnitude of 10^{-10} m^2 s^{-3} both for salinity and heat budgets).

In contrast, Ekman transport is predominantly meridional and therefore an important term for transporting mass. In addition, geostrophic velocity is difficult to estimate in the sea-ice sector, given the sea-ice cover that prevents large-scale estimate of geostrophic flow from satellite altimeter, thus would contain significant errors. We however note that neglecting geostrophic flow might be one source of error in our mixed-layer budgets. We discuss the possible impact below in the discussion section.

We use a spatially constant vertical diffusion coefficient of 10^{-5} m^2 s^{-1} [*Cisewski et al.*, 2005; *Wu et al.*, 2011]. While we believe this is a commonly used and accepted value for vertical mixing coefficient at the base of the mixed-layer [*Marshall et al.*, 1999; *Karsten and Marshall*, 2002; *Sallée et al.*, 2010], it remains much uncertainty on such values. We note, however, that the presence of sea-ice undoubtedly insulate the mixed layer from atmospheric disturbance, which would argue for a diffusion coefficient at the lower bound of what is generally discussed for the majority of the ocean.

The entrainment velocity is calculated following *Ren and Riser* [2009]:

$$w_e = H\left(\frac{\partial h_m}{\partial t}\right), \tag{8}$$

where:

$$H(x) = \begin{cases} 1, & \text{if } x \geq 0 \\ 0, & \text{if } x < 0. \end{cases} \tag{9}$$

The salinity and temperature differences across the base of the mixed layer are computed as the difference between the average salinity or temperature within the mixed layer and 15 m below the determined base of the mixed layer. The choice of the salinity or temperature reference depth at 15 m below the mixed layer is based on analysis from *Ren et al.* [2011].

Description of Ekman transport and net heat and freshwater fluxes are provided below.

2.7. Ekman Transport

Ekman transport can be computed from wind stress, assuming the mixed-layer depth is deeper than the Ekman layer:

$$U_e = \frac{1}{\rho_0 f h_m}\begin{pmatrix} \tau^y \\ -\tau^x \end{pmatrix}, \tag{10}$$

where f is the Coriolis parameter, ρ_0 is the reference density of seawater, τ^y and τ^x are, respectively, the zonal and meridional wind stress.

The local wind stress felt by the ocean surface can be modulated by the presence of sea-ice: the surface momentum flux comes then from both air/sea and ice/sea stresses and therefore, in this study, we consider the sea-ice cover in our calculation of the stress felt by the ocean surface layer, as following:

$$\tau_{tot} = \begin{pmatrix} \tau^x \\ \tau^y \end{pmatrix} = \begin{pmatrix} (1-A_{ice})\tau^x + A_{ice}\, C_D\, |u_{ice}|u_{ice} \\ (1-A_{ice})\tau^y + A_{ice}\, C_D\, |v_{ice}|v_{ice} \end{pmatrix}, \tag{11}$$

where A_{ice} is the percentage of ice cover, C_D is the ice drag coefficient fixed at 5×10^{-3} [*Goosse and Fichefet*, 1999; *Vancoppenolle et al.*, 2009], u_{ice} and v_{ice} are, respectively, the meridional and zonal ice velocity assumed to be equal to 2% of the wind velocity [*Thorndike and Colony*, 1982] (note that the choice of this 2% coefficient has a very small sensitivity on the resulting net Ekman transport contribution).

The Ekman transport is computed from equations (10) and (11), using the NCEP CFSR atmospheric reanalysis over the period 2000–2010 (http://cfs.ncep.noaa.gov/cfsr/docs/).

2.8. Net Heat and Freshwater Fluxes

The atmospheric freshwater flux as well as the under-ice forcing and the heat flux into the mixed layer are used to compare seasonal change of buoyancy in the surface layer and forcing by air and sea-ice fluxes.

In this paper, we use air-sea-ice fluxes from five different products either based on numerical model simulations or based on sea-ice observations and atmospheric reanalysis. Specifically we use: two observation-based data sets produced by *Tamura et al*. [2011], which are forced by atmospheric forcing from either NCEP or ERAint reanalysis (hereafter denoted *Tamura (NCEP)* and *Tamura (ERA)*); one data set, which is an output from a mixed-layer model coupled to the sea-ice model CICE [*Petty et al*., 2014] (hereafter denoted *Petty (CICE)*); one data set, which is an output from an ocean model (NEMO3.5) coupled to the sea-ice model LIM3.6 [*Barthélemy et al*., 2016] (hereafter denoted *Barthélemy (LIM)*); and a final data set from an observation-based reanalysis product by *Haumann et al*. [2016, hereafter *Haumann*]. Each of these products provide us with both net freshwater fluxes felt into the ocean (FWF) and net heat flux into the ocean (Q_{net}), except for the product from *Haumann et al*. [2016] which only provides freshwater flux. We can write each of these fluxes as a contribution to a net buoyancy flux into the ocean, following:

$$B_{FWF} = g\beta \times S_m\, FWF, \tag{12}$$

$$B_{Qnet} = g\alpha \times \frac{Q_{net}}{\rho_0 C_p}, \tag{13}$$

Similarly, we convert all the terms of equation (6) and (7) into buoyancy content change induced by heat or freshwater. Therefore, all units of the mixed-layer budgets are in buoyancy flux unit m^2/s^3, which allows to quantitatively compare the respective contribution of heat and freshwater to the ocean buoyancy content. The convention used in this study is that positive buoyancy flux corresponds to a water mass that becomes more buoyant because it becomes fresher or warmer.

These fluxes have been chosen as they have been designed with the aim of resolving freshwater fluxes in the sea-ice sector. All of these fluxes include freshwater fluxes arising from ocean/sea-ice interactions. The two coupled model products (*Petty (CICE)* and *Barthélemy (LIM)*) also include the precipitation/evaporation flux at the ocean surface, but we note that in these two products the shape of the seasonal cycle is entirely dominated by ocean/sea-ice fluxes. All of these products neglect freshwater fluxes associated with iceberg and ice-shelves.

3. Results

The spatiotemporal complementarity of seals, Argo, and ship profiles allows us to map the seasonal evolution of the surface mixed layer (ML) over the entire Southern Ocean including the seasonally capped sea-ice sector. In this section, after presenting the regional structure of mixed-layer properties, such as mixed-layer depth, salinity, and temperature, we investigate the seasonal evolution of the stratification, as well as the buoyancy forcing, which both ultimately control the seasonal changes of the mixed layer.

3.1. Seasonal Variation of Mixed-Layer Properties

Mixed-layer temperature and salinity exhibit distinct seasonal cycles (Figure 3; see associated errors in Appendix A). Overall, the regional structures of these seasonal cycles organize around two main large-scale characteristics of the Southern Ocean: the Antarctic Circumpolar Current and the seasonal sea-ice covered regions. The fronts of the ACC act as a frontier separating water masses of different properties [*Orsi et al*., 1995; *Sallée et al*., 2008]. Consistent, our results show very distinct water mass in the surface layer north and south of the ACC that vary strongly in properties: warmer and saltier in the subtropics, north of the ACC, than in the subpolar region, south of the ACC. Past observation-based studies on the Southern Ocean mixed layer have generally focused on regions within and north of the ACC [*Sallée et al*., 2006; *Dong et al*., 2007, 2008, 2009; *Ren et al*., 2011], while much less attention have been devoted to the subpolar regions due to the lack of large-scale observational data set. Here we mostly focus on the subpolar regions.

In the subpolar regions, temperature and salinity are closely linked to the seasonal sea-ice cover, with the development of the sea-ice cap being associated with a cooling and salinification of the ocean surface layer (Figure 3). During the freezing season, from February/March to October, under-ice mixed-layer temperatures are very homogeneous over the entire circumpolar belt at a temperature close to the surface freezing temperatures (≈ -1.8°C), with little large-scale variation. North of the seasonal sea-ice sector, the ACC fronts are associated with warmer waters, of about 2–3°C at the Polar Front. The seasonal growth of sea-ice cover induces a modulation of the meridional temperature gradient directly north of the sea-ice sector, with an

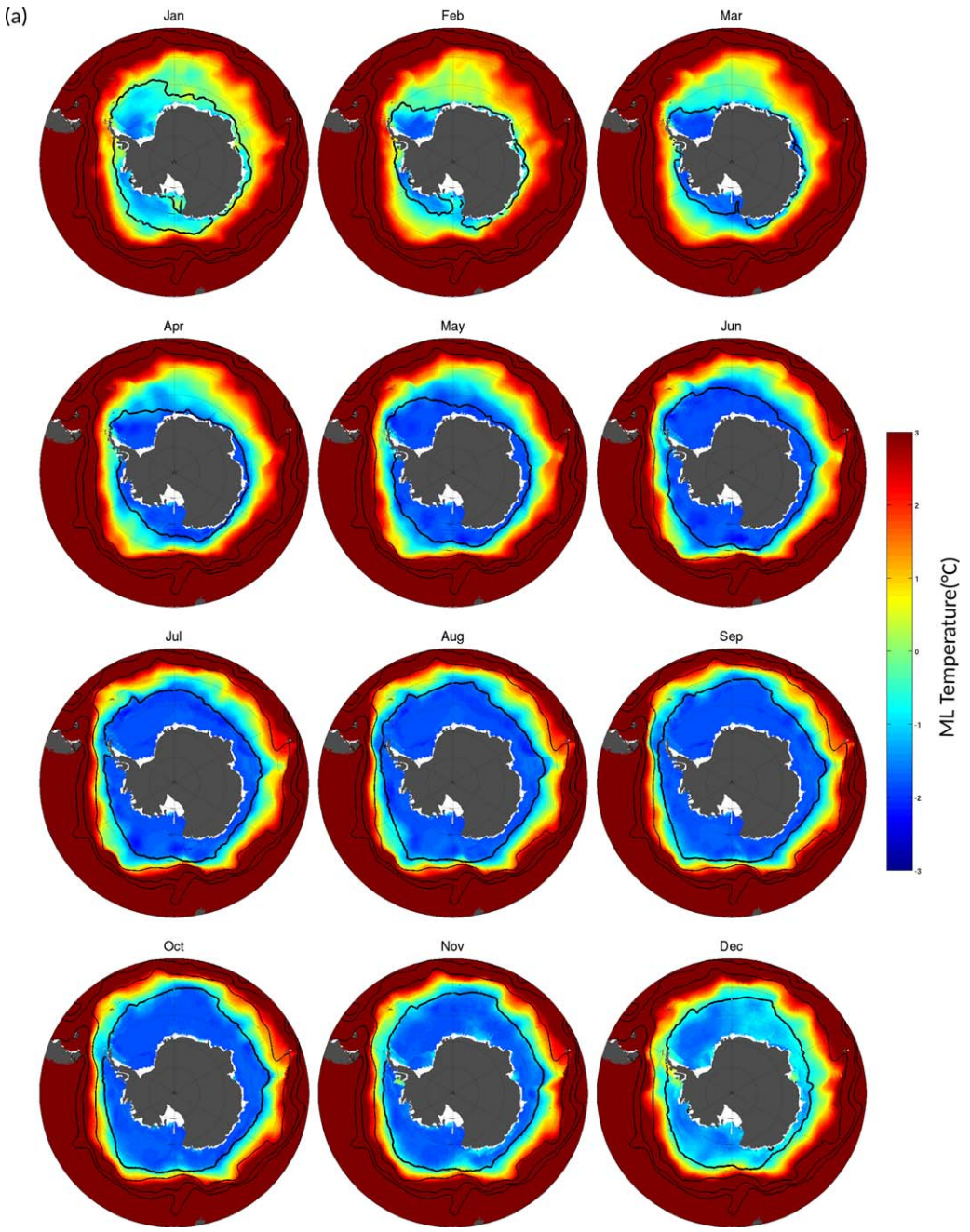

Figure 3. Monthly evolution of the mixed-layer (a) temperature and (b) salinity over the entire Southern Ocean. Fine black lines represent the main fronts of the Antarctic Circumpolar Current (i.e., SAF northward and PF southward) whereas the thick black line corresponds to the maximum seasonal sea-ice extension.

intensification of the meridional temperature gradient in winter, when cold under-ice surface waters extend close to the warmer Polar Front surface waters.

In contrast to the somewhat spatially homogenized under-ice mixed-layer temperature, the under-ice mixed-layer salinity exhibits a large regional variability (Figure 3b). Overall, subpolar mixed-layer salinity has a seasonal cycle in phase with sea-ice extent or mixed-layer temperature: salinity increases from February/March to October, before rapidly decreasing during melt season from November to January/February. Though the amplitude of the seasonal signal shows large regional differences. The amplitude reaches its maximum around the Antarctic Peninsula, Weddell Sea, Ross Sea, and along the edge of the

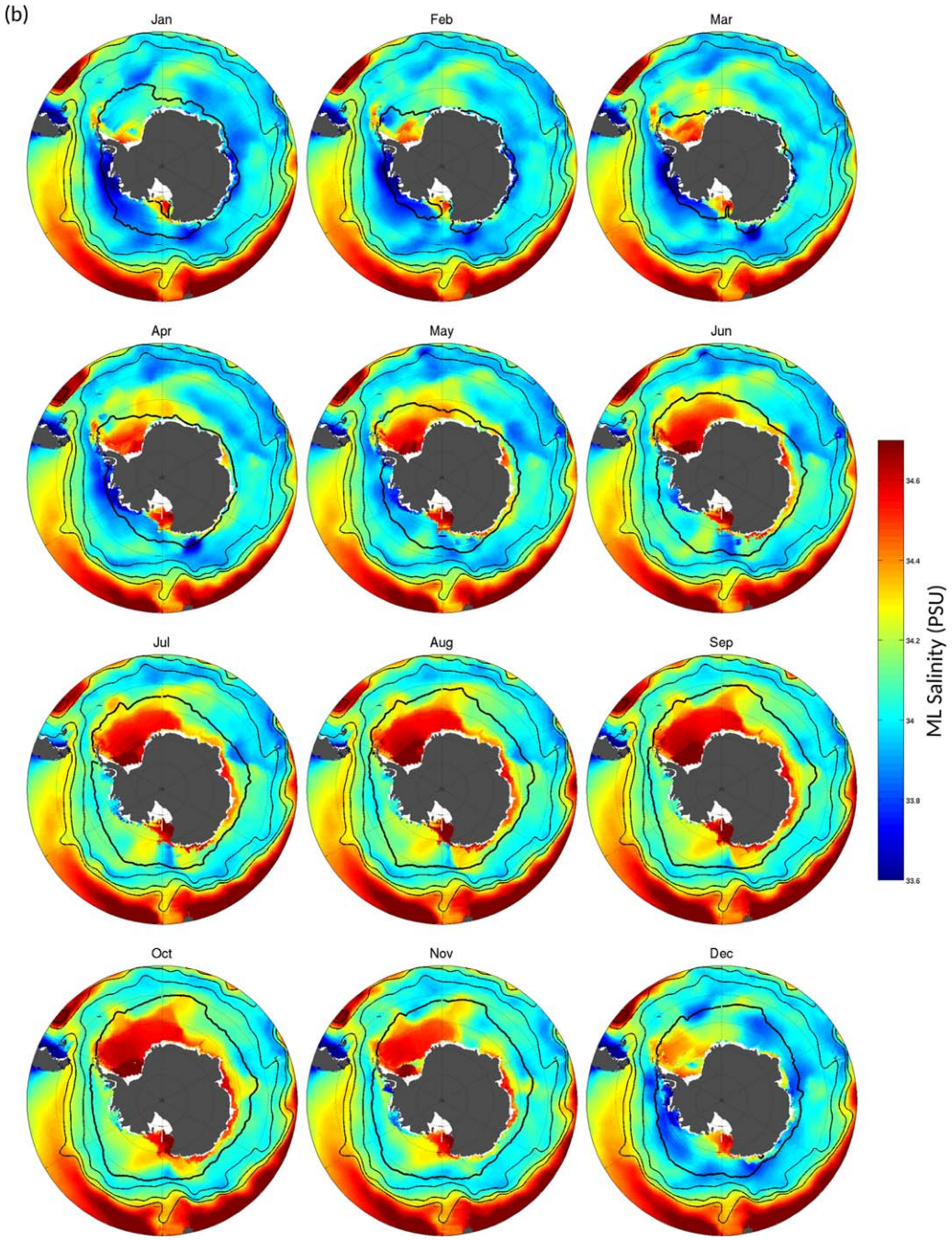

Figure 3. (continued)

East Antarctica coast. In these regions, the amplitude of the seasonal cycle can be as high as 0.8 g kg^{-1}, ranging from about ~33.8 g kg^{-1} to about ~34.6 g kg^{-1} (Figure 3b). The regional structure of the salinity cycle in the sea-ice zone qualitatively agrees with the broad circulation of the Antarctic subpolar oceans. Away from western Peninsula, a large meridional salinity gradient develops in winter under sea-ice at the Antarctic Shelf break. This salinity gradient consistent with intense fall/winter brine rejection associated with sea-ice formation, translates into a density gradient (temperature being homogenized; Figure 3) at the shelf break.

Due to the spatially homogeneous temperature, the under-ice seasonal evolution of mixed-layer density is tightly linked to seasonal cycle of salinity, with a winter densification of the mixed layer, which is associated

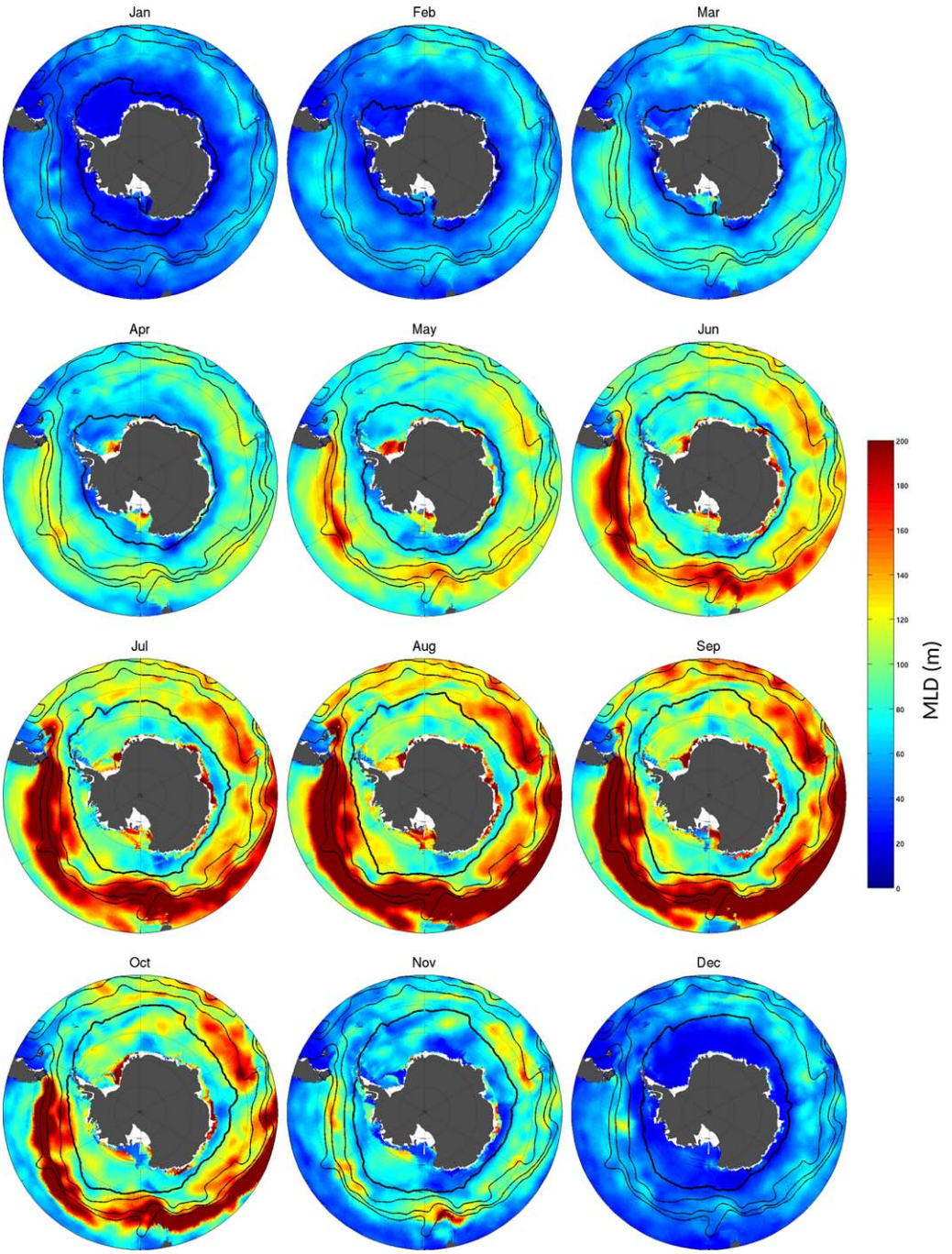

Figure 4. Monthly evolution of the mixed-layer depth in the Southern Ocean. Fine black lines represent the main fronts of the Antarctic Circumpolar Current whereas the thick black line corresponds to the maximum seasonal sea-ice extension.

to the deepening of the ML by convective processes (Figure 4; see associated errors in Appendix A). Under sea-ice the mixed layer deepens from tens of meters in summer to more than 200 m during winter. However, the deepest under-ice mixed layers of more than 200 m are very localized to the shelves and the shelf break (Figure 4; August/September maps). On individual profiles, winter mixed layer at the shelf break were found locally to be as deep as 300–500 m. In winter, north of these deep localized mixed layers, a circumpolar band of relatively shallow mixed layer (∼50–100 m) extends up to the marginal sea-ice zone. Then, north of the marginal sea-ice zone, mixed layer deepens toward the ACC to reach the very deep convection area associated with the formation of intermediate and mode water north of the ACC [e.g., *Sallée et al.*, 2008;

Dong et al., 2008] (Figure 4). This meridional structure in the depth of the winter mixed layer suggests that sea-ice has a role of isolating and stabilizing the upper-ocean except close to the continent where more ice might form in coastal polynyas and/or open areas developing between the pack and fast ice [e.g., *Massom and Stammerjohn*, 2010]. After reaching their maximum depth in August/September, under-ice mixed layers restratify rapidly to depths of only few tens of meters.

3.2. Stratification at the Base of the ML and Buoyancy Content Change

The monthly climatological maps of temperature, salinity, and depth presented above show very marked seasonal cycles in the entire Southern Ocean. However, the sea-ice sector appears to be associated with its own specific dynamics. In this section, we aim at describing these specific differences between sea-ice sector and ice-free regions. As such, we first present the seasonal evolution of the stratification of the water column at the base of the mixed layer, which is ultimately associated with the ability to mix, and second, we introduce the seasonal evolution of the mixed-layer buoyancy content.

In both ice-free and sea-ice zone, the stability at the base of the mixed layer has a strong seasonal cycle, with stability being eroded in winter (i.e., approaching the gray shaded area on Figure 5, which represents unstable profiles). The weakening of the stability is associated with a deepening of the mixed layer, which reaches a maximum in August–September before starting to restabilize and shallow. However, the seasonal cycle of the stability at the base of the mixed layer is explained by very distinct temperature and salinity contributions in the two regions.

In the ice-free ocean, the amplitude of the seasonal cycle of the stability at the base of the mixed layer is dominated by its temperature contribution. The amplitude of the seasonal cycle of the temperature contribution to the stability has a range of about 9×10^{-5} s^{-2}, much wider than its salinity-driven counterpart with a seasonal range of about 2×10^{-5} s^{-2} (Figure 5). In contrast, the amplitude of the seasonal cycle of the mixed-layer stability in the sea-ice sector is driven by both temperature (seasonal range of $\sim 6 \times 10^{-5}$ s^{-2}) and salinity contribution (seasonal range of $\sim 8 \times 10^{-5}$ s^{-2}; Figure 5), with a slight domination of the salinity contribution. The amplitude of the temperature-driven signal maximizes from November to May

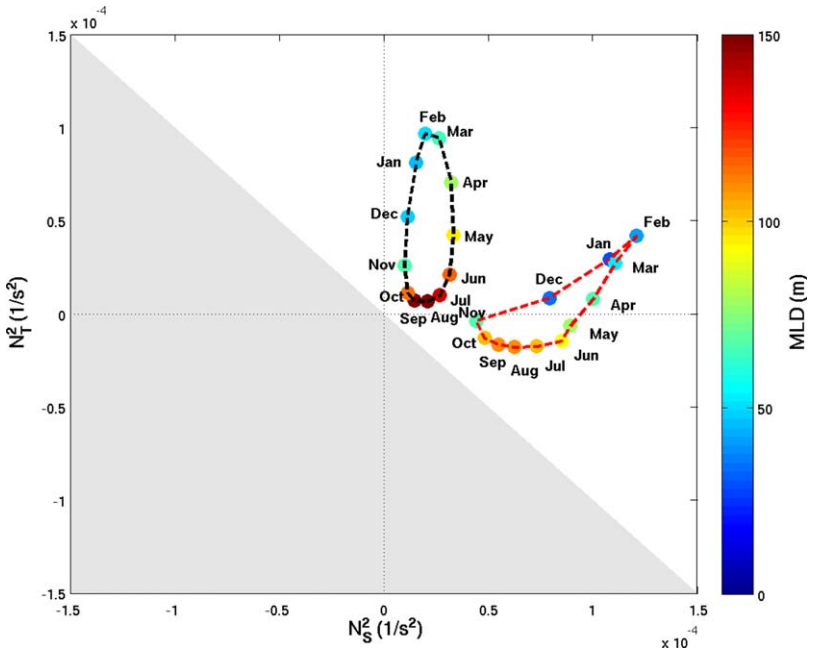

Figure 5. Monthly evolution of the stratification at the base of the ML for the sea-ice region (red line) and the ice-free ocean (black line) in a Turner diagram (see equation (3) for more details). Colored dots represent the mean MLD over the given month. The gray zone corresponds to a gravitationally unstable stratification of the water column. Then the stability properties of the stratification are divided into three situations: positive N_S^2 and negative N_T^2 when a destabilizing temperature gradient is accompanied with a stabilizing salinity gradient; both positive N_S^2 and N_T^2 when temperature and salinity gradients have the same contribution in stabilizing the water column; negative N_S^2 and positive N_T^2 when a destabilizing salinity gradient is accompanied with a stabilizing temperature gradient.

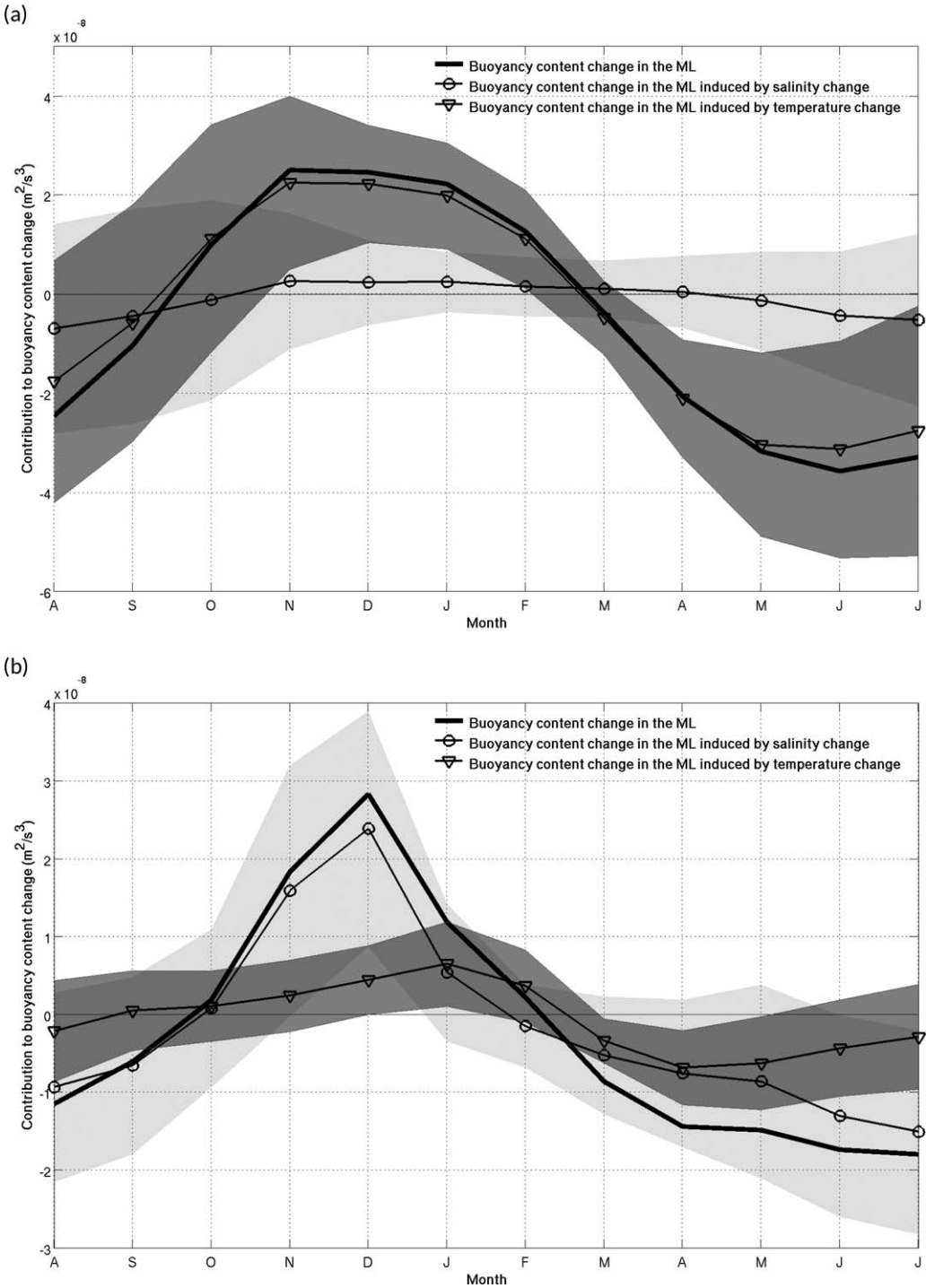

Figure 6. Annual-mean cycle of the buoyancy content change within the ML in (a) ice-free and (b) sea-ice zone. The thick black line shows the monthly evolution of the buoyancy content change in the ML, the fine lines represents the contribution of the salinity content change (circles), and the contribution of the temperature content change(triangles). Units are m^2/s^3. Gray shadings correspond to standard deviation of monthly means for each component. The time series begins in August.

when the sea-ice cap does not cover the entire sector, allowing surface heat forcing to erode the temperature-driven stability. However, in winter, from May to November, the stability is almost exclusively governed by its salinity-driven contribution. The dominance of the salinity stability on the seasonal amplitude of the mixed-layer stability is even more obvious when limiting the region to the Antarctic shelves

seas, representing the areas with near year-round ice covers with sparse polynyas (amplitude of salinity stability is about four time greater than the amplitude of temperature stability over the annual cycle; not shown).

It is interesting to note that during winter in the sea-ice sector (Figure 5), the temperature profile is unstable consistent with the strong overall cooling of the surface layer (Figure 3a) overlying the warmer Warm Deep Water [*Gordon and Huber*, 1990]. The overall stability of the mixed layer in winter in the sea-ice region is sustained by the stability of the salinity profile, which counterbalances the instability of the temperature profile, though it erodes slowly as winter progresses.

The seasonal erosion of temperature and salinity stratification at the base of the mixed layer is associated with seasonal buoyancy content change inside the mixed layer. Similar to stratification, we decomposed the buoyancy content change into a temperature and haline contribution (Figure 6). Consistent with the stability at the base of the mixed layer, the mixed-layer buoyancy content change is strongly dominated by its temperature contribution in the ice-free sector (Figure 6a), and by its haline contribution in the sea-ice sector (Figure 6b). Overall, both regions gain buoyancy from about October to February and loose buoyancy the rest of the year. However, the shape of the buoyancy content change time series strongly differ between ice-free and sea-ice sector (Figure 6). The forcing of the seasonal evolution of the buoyancy content change has been widely discussed in the ice-free sectors in previous studies, thus we refer to these for further details [e.g., *Sallée et al*., 2006; *Dong et al*., 2007, 2008, 2009; *Ren et al*., 2011]. We investigate for the first time this evolution from observational data in the sea-ice sector on a circumpolar scale. We tackle the question of the forcing of the seasonal buoyancy content change in the sea-ice sector in the next section.

3.3. Heat and Salt Mixed-Layer Budget in the Sea-Ice Sector

Variations in the mixed-layer buoyancy content change can originate from a number of processes, including surface fluxes (air-ice-sea), lateral advection, vertical entrainment, and diffusion (see equation (6) and (7)). In this section, we examine each of these terms and quantify their respective impact on the temperature and salinity contribution to the mixed-layer buoyancy content change in the sea-ice sector. We present a heat and salt budget below.

3.3.1. Heat Budget

The averaged quantification of heat budget forcing over the entire sea-ice sector shows a strong dominance of air-ice-sea fluxes compared to the other terms. Vertical diffusion (pink curve on Figure 7a) and lateral advection by Ekman transport (green curve on Figure 7a) are on an order of magnitude smaller than the observed heat-driven buoyancy content change of the mixed layer (black curve on Figure 7a). The seasonal vertical entrainment is however noticeable, maximizing in February–March at the very start of the mixed-layer deepening season. As mixed layer deepens, it does entrain the cold previous winter remnant Winter Water, which reduces the thermal buoyancy content of the mixed layer. Later in the season, from May to September, the mixed layer continues deepening, but then entrains warmer water (the temperature profile is unstable; Figure 5), entraining underlying CDW often called Warm Deep Water (WDW) [e.g., *Gordon and Huber*, 2016]. The envelope defined by the four air-ice-sea flux products used in this study suggests that surface air-ice-sea forcing maximizes in January with a mean surface warming contribution of about $0.8-1.5\times10^{-8}m^2s^{-3}$, and minimizes in fall in April/May with a mean surface cooling contribution of about $0.5-0.8\times10^{-8}m^2s^{-3}$. The largest cooling in the sea-ice zone occurs in fall due to the evolution of the seasonal ice cover, which isolates the ocean from large atmospheric heat loss in winter. The sum of the forcings considered here agrees well with the observed seasonal change of heat-driven buoyancy content change (Figure 7b).

3.3.2. Salt Budget

Similar to the heat budget, forcing terms of the salt budget are quantified over the sea-ice sector. Lateral advection by Ekman transport and diffusion are found negligible, and in agreement with the derived heat budget, we find that the two main contributors to the salt budget are entrainment and air-ice-sea forcing (Figure 8). The vertical entrainment is as important as air-ice-sea forcing for the period February–June. From late fall onward, the deepening of the mixed layer entrains the underlying WDW into the mixed layer, which are saltier than the mixed layer, therefore decreasing the overall buoyancy content of the mixed layer (in agreement with the stable salinity profile described in previous sections; Figure 5).

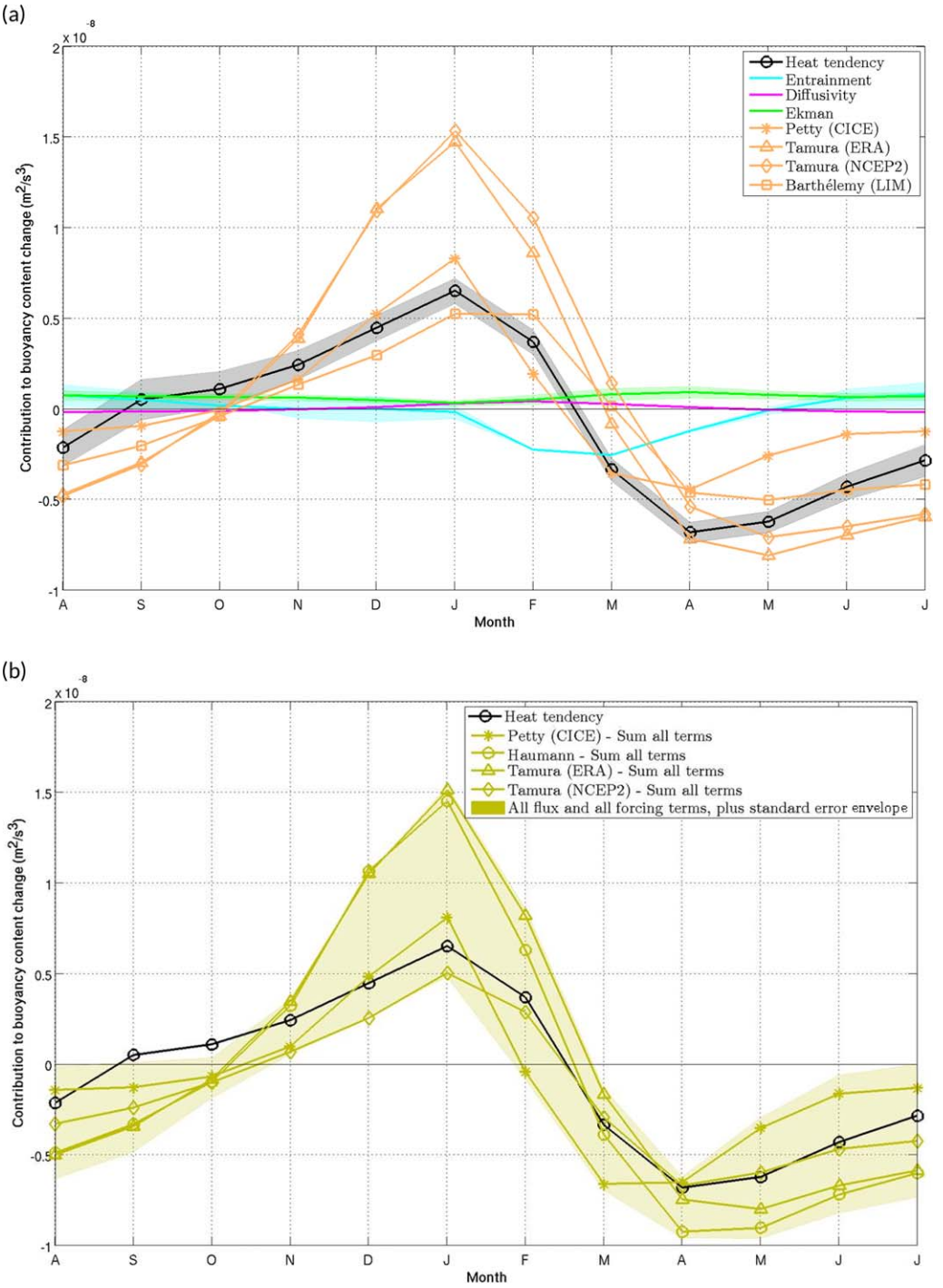

Figure 7. (a) Annual-mean cycle of the forcing terms controlling the ML heat balance in sea-ice zone (see equation (7) for more details). The black line shows the monthly evolution of the heat content in the ML from the observations, the purple line shows the vertical eddy diffusivity, the cyan line represents the entrainment at the base of the ML, and the green line shows the Ekman advection. Finally, orange lines represent the surface heat flux into the ML estimated from various models. (b) Temperature tendency versus sum of forcing terms into the ML estimated from various models, all in sea-ice zone. In contrast to Figure 6, where shading shows internal variability, shading in this figure shows errors associated with each component (propagated from instrumental errors, interpolation, etc.; see Appendix A). Units are m^2/s^3. The time series begins in August.

The envelope defined by the five air-ice-sea forcing products suggests a gain of buoyancy from October to February/March, and maximizing in December at $1.3-3.5\times10^{-8}m^2s^{-3}$. It is interesting that all of the five different air-ice-sea forcing estimates used in this study agree well with each

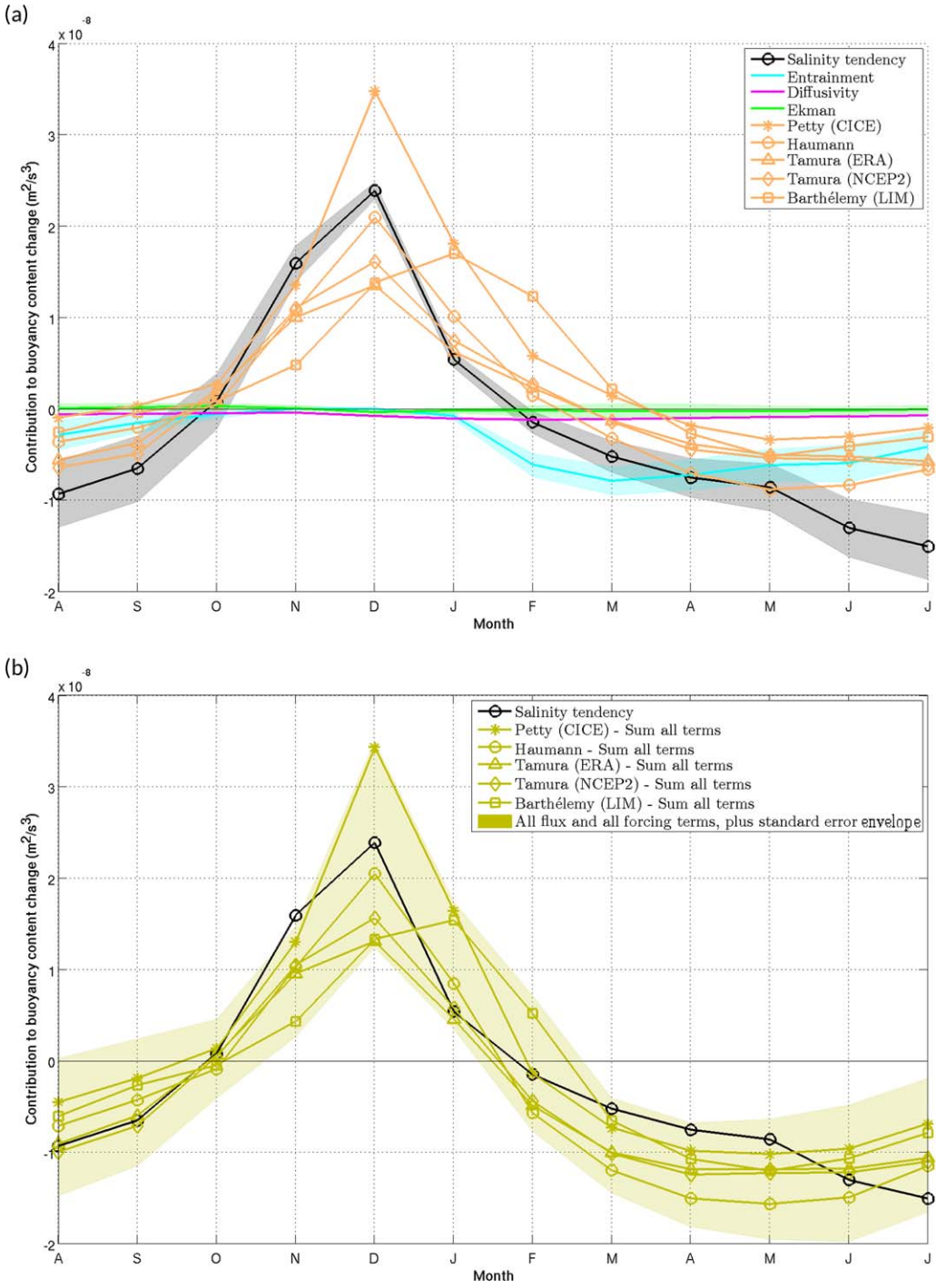

Figure 8. (a) Annual-mean cycle of the forcing terms controlling the ML salinity balance in sea-ice zone (see equation (6) for more details). The black line shows the monthly evolution of the salinity content in the ML from the observations, the purple line shows the vertical eddy diffusivity, the cyan line represents the entrainment at the base of the ML, and the green line shows the Ekman advection. The freshwater flux into the ML estimated from various models is represented by the orange lines. (b) Sum of forcing terms versus salinity trend into the ML estimated from the models, in the sea-ice zone. In contrast to Figure 6, where shading shows internal variability, shading in this figure shows errors associated with each component (propagated from instrumental errors, interpolation, etc.; see Appendix A). Units are m^2/s^3. The time series begins in August.

other. Thus, it is helpful to looking into how much their spatial patterns agree with another. Figures 9c–9l show the regional comparison of the different air-ice-sea forcings, showing the local sum of all months where local fluxes are positive, the melt season, and the map of the local sum

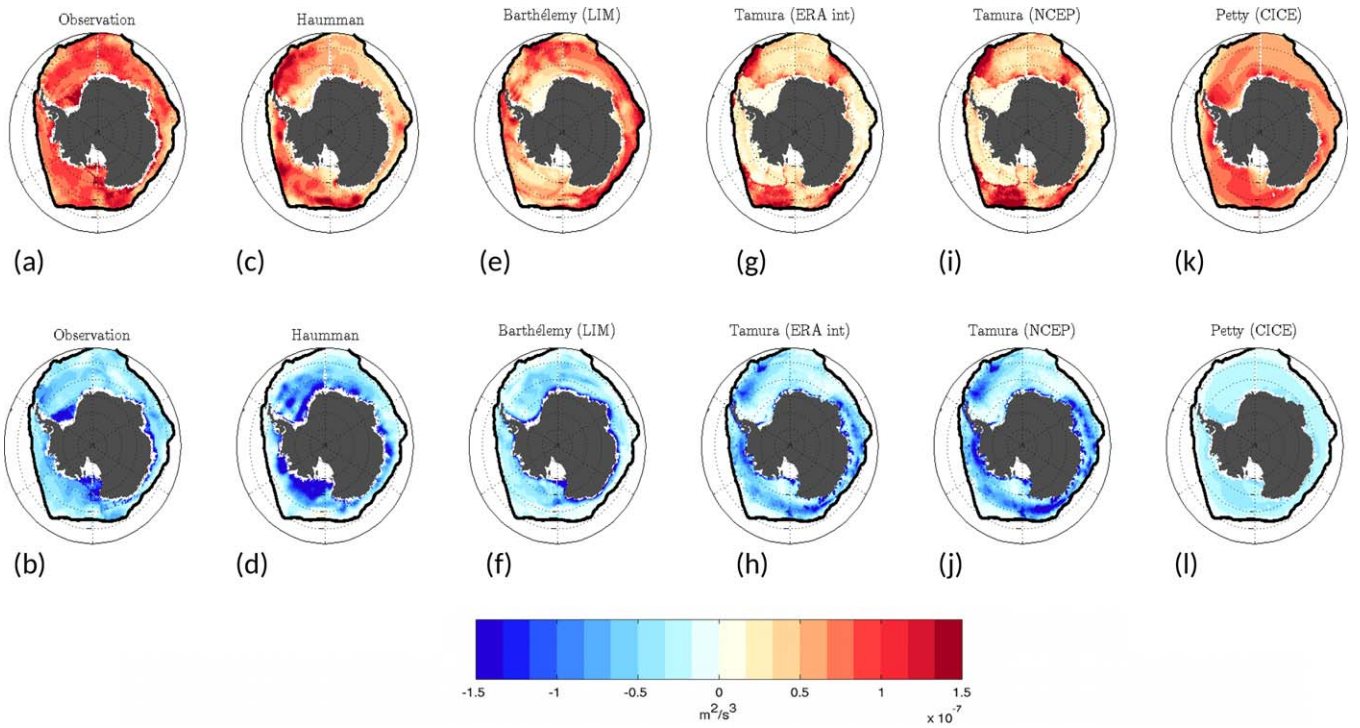

Figure 9. Summer and winter air-ice-sea forcing estimates from observations and five models. (top) The locally integrated positive fluxes, i.e., the period of sea-ice is melting, and (bottom) the locally integrated negative fluxes, i.e., the sea-ice is in formation period. These air-ice-sea forcing estimates show (a, b) observations, (c, d) Haumann, (e, f) Barthélemy, (g, h) Tamura with ERA-int, (i, j) Tamura with NCEP, and (k, l) Petty. All terms in m^2/s^3.

of all months where local fluxes are negative, the freezing season. In this way, we isolate fluxes associated to brine rejection (i.e., negative buoyancy fluxes; associated with ice formation), and fluxes associated to freshwater input (i.e., positive buoyancy fluxes; associated with ice melt). Regionally, the brine rejection and ice melt fluxes estimated from the five different air-ice-sea products used in this study show very large spread. For comparison, we also show the ocean observation-based estimate of air-ice-sea forcing ($\widetilde{FWF}$) by changing equation (6) to:

$$\widetilde{FWF} = \frac{\partial S_m}{\partial t} + U_m.\nabla S_m - \kappa\frac{\partial S_m}{\partial z} + \frac{w_e \Delta S_m}{h_m}. \tag{14}$$

While neglecting lateral advection by geostrophic currents on a local scale might not be valid (compared with the circumpolar-scale budget we presented above), $\widetilde{FWF}$ gives us an indication of the regions most affected by brine rejection and ice melt fluxes. Our estimate of $\widetilde{FWF}$ based on equation (14) suggests that brine rejection is very localized to the Antarctic shelf and shelf break, with maximums in the Weddell, East Antarctic, and Ross sectors (Figure 9b). This is in accordance with satellite-based studies analyzing ice formation and polynyas around Antarctica [e.g., *Tamura et al.*, 2008]. Further offshore, estimated brine rejection is much smaller though not negligible. In contrast, the estimated freshwater input associated with ice melt is much more spread (Figure 9a), occurring over the entire sea-ice covered area.

4. Discussion and Conclusion

The seasonal cycle of mixed-layer properties is described over the entire Southern Ocean using more than 465,000 hydrographic profiles (including 100,000 in the sea-ice sector). In particular, the 10 year database of hydrographic profiles from instrumented southern elephant seals [*Roquet et al.*, 2014] allows us to unveil

the seasonal cycle of the mixed layer in the seasonally capped sea-ice sector. The error associated to our mixed-layer properties climatology comes from two main sources discussed in Appendix A: error on the mixed-layer depth detection which we estimate to be lower than 25%, and sampling error. As displayed in Figure 1, while sampling is unprecedented high in the sea-ice sector, it is uneven and can be regionally poor (e.g., middle of the Ross Sea gyre).

The properties of the Southern Ocean mixed layer undergo a strong seasonal cycle. The under-ice mixed-layer deepens and cools to about freezing point, while becoming saltier in winter. While the buoyancy content change in the ice-free ocean is dominated by temperature change, we show that the seasonal cycle in buoyancy content is mainly driven by salinity changes in the sea-ice sector (Figure 6). Underneath sea-ice, salinity strongly increases in winter in the Weddell and Ross Sea sectors, as well as along the eastern Antarctic coast (Figure 3b) [*Tamura et al*., 2008]. The under-ice increase of salinity is primarily driven by air-sea-ice fluxes (Figure 8), which suggests that sea-ice formation regionally maximizes in the Weddell and Ross Sea sectors and along the eastern Antarctic coast in typical polynya locations (Figure 9). These regions of potentially large sea-ice formation are consistent with the regions of coastal polynyas known to form large amounts of sea-ice around the Antarctic coast [e.g., *Markus et al*., 1998; *Massom et al*., 1998; *Tamura et al*., 2008]. The local enhanced increase of salinity in the vicinity of the Antarctic shelf is associated with a densification of the mixed layer. The shelf break is therefore associated with an increase of its meridional density gradient in winter, which points to a likely seasonal modulation of the Antarctic Slope Current [e.g., *Mathiot et al*., 2011]; we note, however, that focusing over the entire water column, rather than only in the mixed layer, would be needed for better understanding of this possible link).

Our results suggest the coastal regions with high sea-ice formation are also associated with a maximum ice export confirming works based on satellite observations [e.g., *Holland and Kwok*, 2012; *Haumann et al*., 2016]. Other studies estimate that about 40% of the sea-ice formed in Weddell Sea (70% in Ross Sea) is exported northward by wind-driven advection [*Petty et al*., 2014]. Further offshelf, on an annual time scale, the ocean is impacted more by the freshwater input from sea-ice melt (i.e., the surface layer tends to be stabilized) than from the brine rejection which is mostly modulating the mixed layer close to the shelf break (i.e., the surface layer tends to be destabilized; Figure 9). This contrasting effect of sea-ice ocean feedback leads to a meridional banded structure of the winter mixed-layer depth in the Southern Ocean: deep next to the continent; shallow further offshore; and deepening again northward within the ACC (Figure 4). The under-ice mixed-layer depth actually locally maximizes at the shelf break where winter mixed layer interacts with the underlying Warm Deep Water [*Gordon and Huber*, 1990]. While mixed-layer properties at the shelf break are somewhat smoothed out by the interpolating procedure in this climatological analysis, individual profiles show mixed layers as deep as 300–500 m.

Overall, the depth of the mixed layer is a combination of the static stability of the water column and the destabilizing forcing (e.g., atmospheric low, brine rejection, winds). Given that the winter under sea-ice surface layer is cooled to the freezing point in winter (i.e., it reaches the minimum possible temperature; Figure 3a), the stratification of the surface layer in the sea-ice sector is clearly sensitive to the temperature of deep waters, which upwell to shallow depths south of the ACC [*Lumpkin and Speer*, 2007]. The cold surface layer is stable due to its high freshwater content (Figure 5). Consistent, *You* [2002] demonstrated that near Antarctica, the upper layer is thermally unstable which puts it in a diffusive convection regime, whereas north of the ACC, temperature and salinity both contribute to the stabilization of the surface layer, which is therefore in a doubly stable regime. In the sea-ice sector, the effects of freshening and cooling on density virtually offset one another, so that surface waters are typically only slightly less dense than the underlying waters (Figure 5). When brine rejection densifies the surface-layer in winter, the water column can become unstable and mixed-layer deepens rapidly. In other words, the stability of the water column controls the amount of sea-ice that can be formed locally before the water column overturns and entrains warm water from below [e.g., *Martinson and Iannuzzi*, 1998], limiting further sea-ice formation.

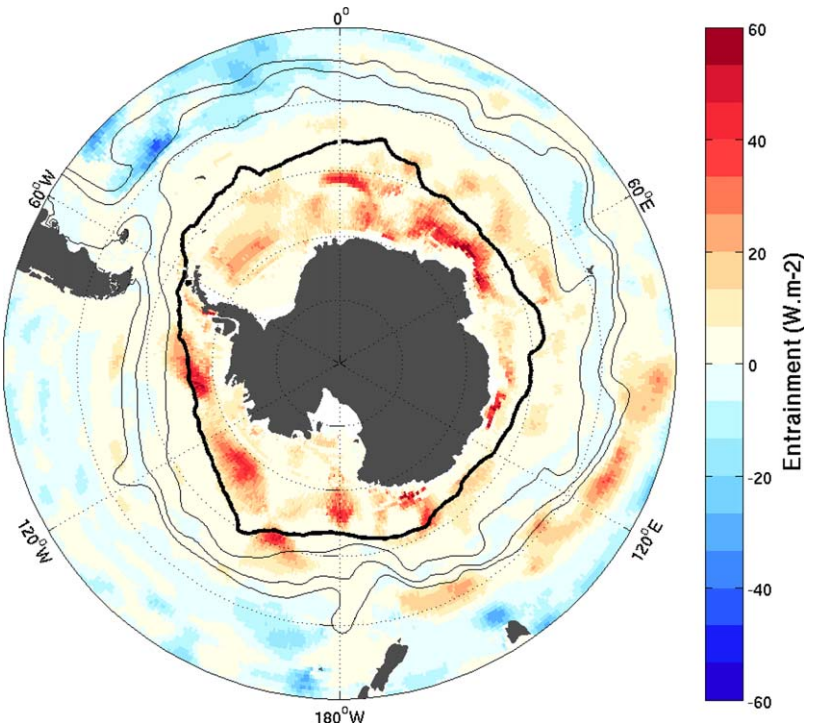

Figure 10. August entrainment of heat in W m^2 and maximum sea-ice extension (thick black line). Fine black lines represent the main fronts of the Antarctic Circumpolar Current.

In the sea-ice sector, the temperature profile at the base of the mixed-layer switches from stable to unstable in autumn/winter (Figure 5). Indeed, in autumn/winter, a cold surface layer (Winter Water) is formed and lies above the relatively warmer Upper Circumpolar Deep Water (UCDW), which leads to unstable temperature profile. In contrast, in spring and summer, as sea-ice melt, the upper ocean warms, leaving a cold water layer (the remnant winter water) in between the relatively warm mixed layer and the relatively warm Upper Circumpolar Deep Water (UCDW). In consequences, as the mixed layer deepens it first entrains cold water from the remnant winter water layer, and then warm waters from the underlying Deep Water. Consistent, we find that after a first phase of cold water entrainment from January to May (i.e., loss of buoyancy; Figure 7a), the surface layer entrains warm water from May to October (i.e., gain of buoyancy; 7a). Incorporation of Deep Water into the winter mixed layer introduces both heat and salt into the surface layer, and thus has a strong impact on the mixed-layer air-sea exchanges and sea-ice formation processes [*Gordon and Huber*, 1990]. This entrainment of heat is critical in a balance of controlling the amount of sea-ice that is locally produced, and modulates the probability of appearance of open ocean polynya [*Gordon*, 1991; *Gordon et al*., 2007]. Our results show an entrainment of 20–60 W m^{-2} at the shelf break in winter (Figure 10), in good agreement with earlier estimates of ~41 W m^{-2} [e.g., *Gordon and Huber*, 1990; *Keeling and Visbeck*, 2011]. This entrainment provides an efficient pathway for exchange of heat, freshwater, as well as air-sea gas exchange (e.g., carbon dioxide, oxygen) between the deep ocean and the atmosphere [*Gordon*, 1991; *Sigman and Boyle*, 2000], which makes the Antarctic sea-ice sector surface layer and its associated weak stability a critical feature of the global climate system [*Sigman et al*., 2010]. It is interesting to note that this system is sensitive to small changes in water mass properties: a surface salinity increase as small as 0.1 (NS change of $\sim 0.5 \times 10^{-4}$ s^{-2}) or a deep water temperature increase as small as 0.5°C (NT change of $\sim 0.3 \times 10^{-4}$ s^{-2}) would be sufficient to eliminate the wintertime stratification (Figure 5).

A number of previous studies suggest that in a context of global warming, the mixed layer is becoming fresher (due to changes in the precipitation-evaporation balance, accelerated melting and calving of Antarctic glaciers and more positive phase of SAM) [*Zhang*, 2007; *Close and Goosse*, 2013; *de Lavergne et al*., 2014]. This freshening of the mixed layer increases the stratification at its base, which in turn reduces the ability for the surface layer to overturn and entrain underlying fluid, and an overall reduction of the deep

ventilation [*Fahrbach et al.*, 2004; *Johnson and Doney*, 2006]. Antarctic convection has an important and climate-relevant role in the formation of the worlds deep waters [*Gordon*, 1991; *Orsi et al.*, 2001; *Johnson*, 2008]. Our study provides a first circumpolar-wide observationally based estimate of the current structure of the properties and stability of the Antarctic surface layer that can be used to assess water mass formation and destruction in the Antarctic oceans, monitor future changes, and assess the ability of models to represent this key region of the global climate system.

Appendix A: Error Estimate

In this section, we discuss the error associated to the seasonal climatological maps of mixed-layer properties. Sources of errors include error in the mixed-layer detection procedure, instrumental errors in measuring temperature, conductivity, and pressure, and potential bias in the spatial sampling.

Defining an error associated with our mixed-layer depth detection procedure is a difficult task, though very important. Various sources of uncertainty enter into our mixed-layer depth detection procedure, e.g., the vertical resolution of the profile, the stratification of the profile, etc. In order to estimate one unique error ϵ_{MLD}, including all sources of uncertainty, we defined the error as the standard deviation of four different methods to estimate MLD: MLD_{Holte}, $MLD_{threshold}$, MLD_{shape}, and $MLD_{gradient}$ (see section 2.2). By construction, our mixed-layer depth detection procedure limits this error, ϵ_{MLD}, to less than 25% of the computed mixed-layer depth (see equation (1)).

The error ϵ_{MLD}, affects not only the MLD, but also the computed mean temperature (T_m) and salinity (S_m) within the mixed layer coming from the MLD detection method. We propagate the error ϵ_{MLD} onto a temperature and salinity error by computing a range span by temperature (ΔT) and salinity (ΔS) when varying the MLD within its computed error envelop. In addition to ΔT and ΔS, error on the mean mixed-layer temperature and salinity are introduced by instrumental error (ξ_T and ξ_S; see Table A1). Altogether, we defined a mixed-layer mean temperature error, ϵ_{T_m}, and a mixed-layer mean salinity error, ϵ_{S_m}, as $\epsilon_{T_m} = \Delta T + \xi_T$ and $\epsilon_{S_m} = \Delta S + \xi_S$.

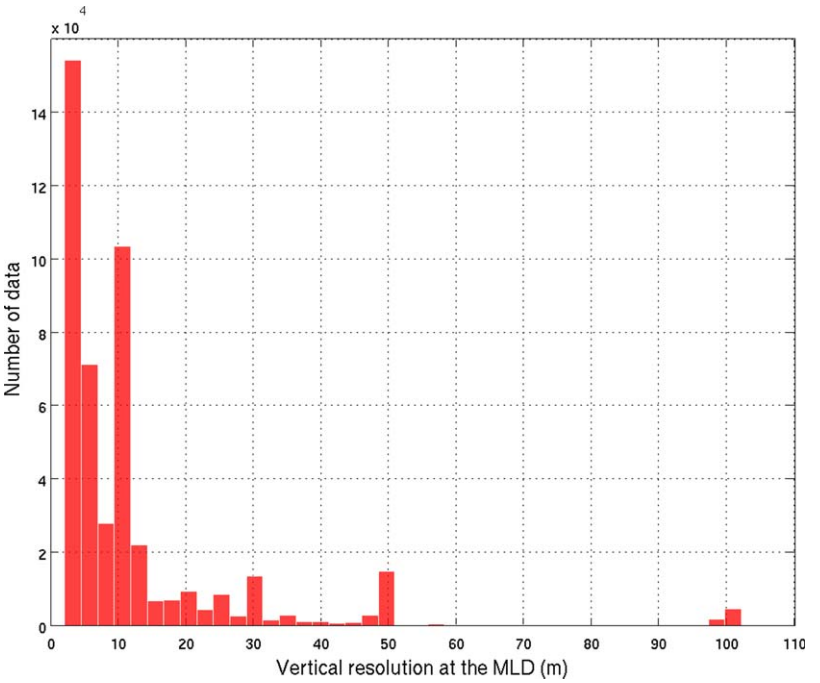

Figure A1. Vertical resolution at the mixed-layer depth (in m), corresponding to the distance between the point above and the point below the MLD estimate.

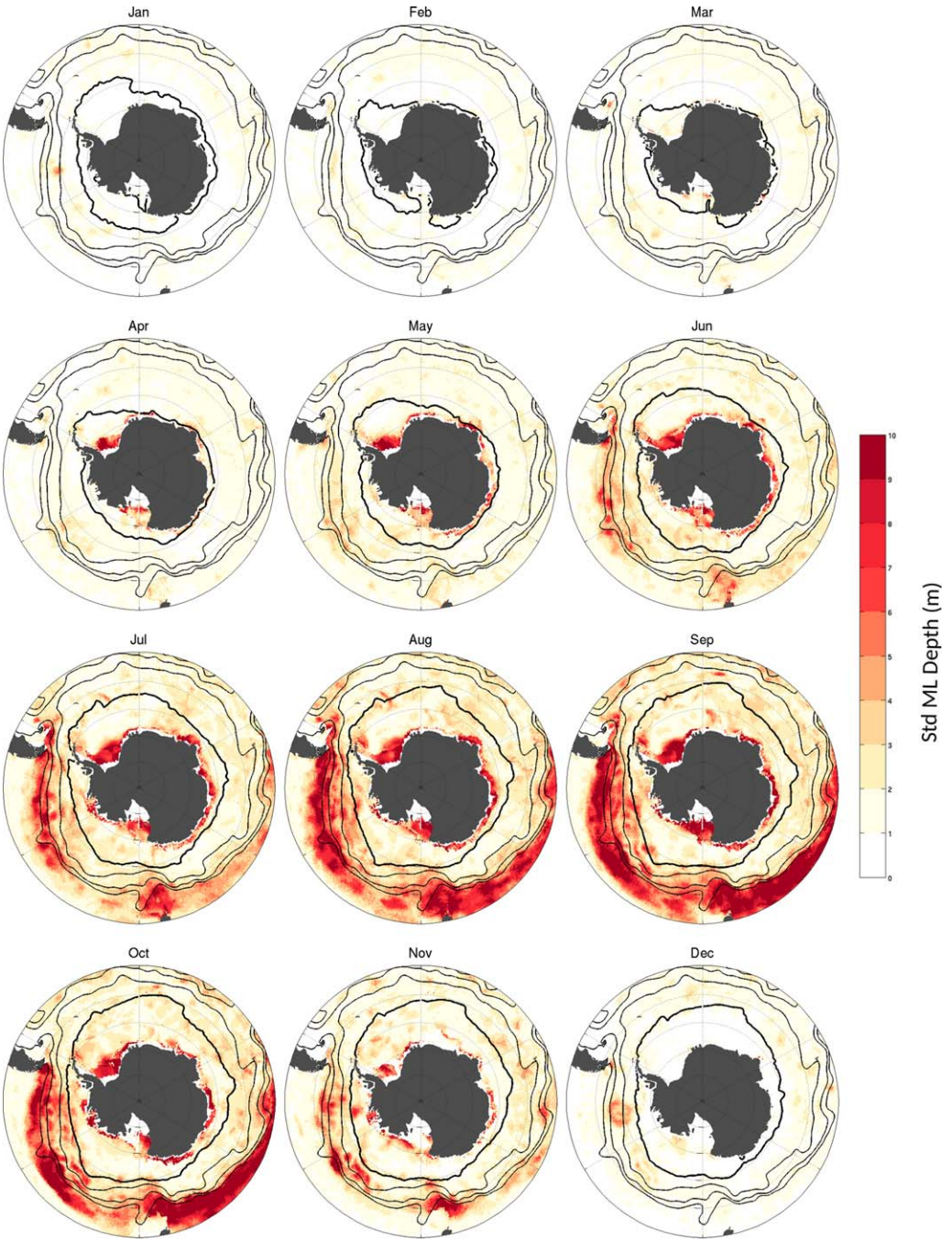

Figure A2. Standard deviation of the mixed-layer depth from the 100 Monte Carlo experiments (in m).

The depth, temperature, and salinity errors computed on each individual profiles (resp. ϵ_{MLD}, ϵ_{T_m}, and ϵ_{S_m}) are propagated through the optimal interpolation procedure with a Monte Carlo experiment. Namely, we repeated a series of 100 different optimal interpolations, in which we randomly attributed small deviations in the input individual mixed-layer depth, temperature, and salinity, within ranges defined by $\mathrm{MLD}_{Holte} \pm \epsilon_{MLD_{Holte}}$, $S_m \pm \epsilon_{S_m}$, and $T_m \pm \epsilon_{T_m}$. The error coming from sampling bias is very difficult to estimate. The best way to get a sense of such error is probably by displaying the observation density map, as done in Figure 1. However, in order to try to quantify such error, we randomly varied the decorrelation scale of the optimal interpolation in the Monte-Carlo experiment.

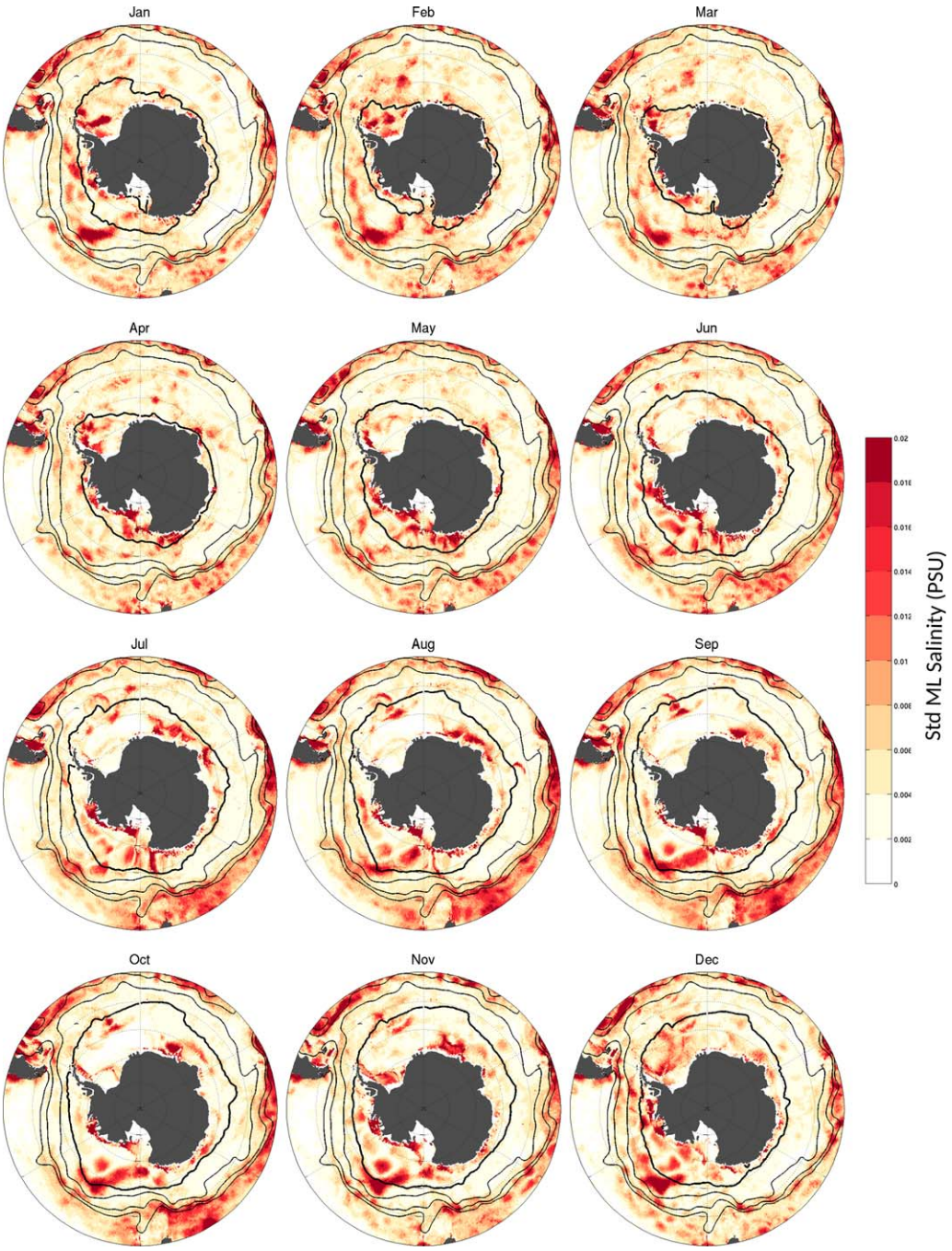

Figure A3. Standard deviation of the mixed-layer salinity from the 100 Monte Carlo experiments (in PSU).

For each month of the seasonal cycle, the standard deviation of the 100 simulations are computed as an estimate of the propagated errors on the climatological seasonal cycle of MLD, and mixed-layer temperature and salinity (Figures A2–A4). Errors maximize in winter in regions where mixed layer is weakly stratified, within the ACC and close to the Antarctic shelves.

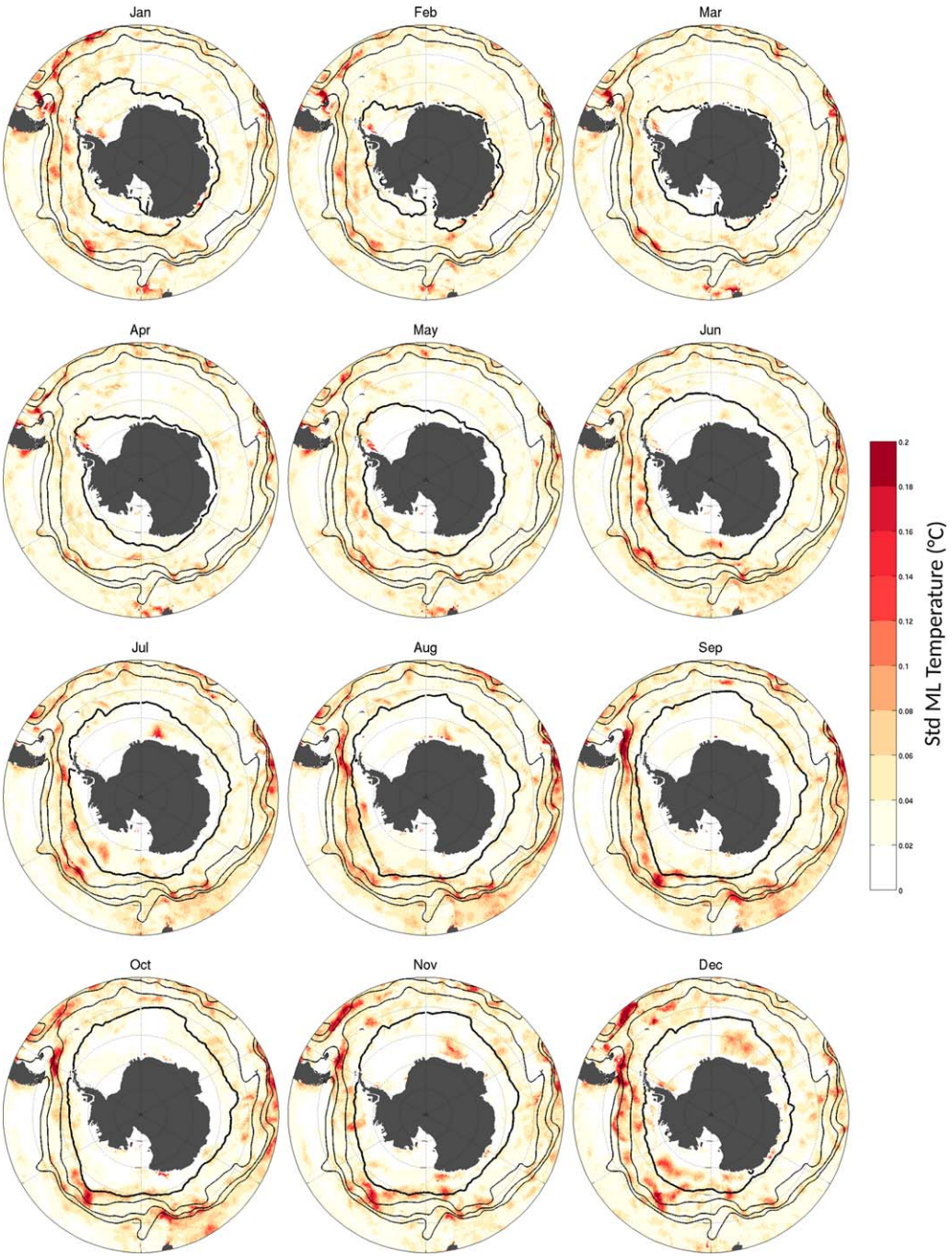

Figure A4. Standard deviation of the mixed-layer temperature from the 100 Monte Carlo experiments (in °C).

Table A1. Typical Instrumental Errors Used in the Error Propagation Procedure

	Temperature (°C)	Salinity (PSU)
Instrumental Error	ξ_T	ξ_S
Argo float profile	0.005	0.01
Ship-based profile	0.002	0.002
Elephant seal profile	0.03	0.05

Acknowledgments
This project has received funding from the European Research Council (ERC) under the European Union's Horizon 2020 research and innovation program (grant agreement 637770). The authors thank M. Petty, M. Barthélemy, M. Tamura, and M. Haumann for providing air-ice-sea data set. Argo data were collected and made freely available by the International Argo Program and the national programs that contribute to it (http://www.argo.ucsd.edu, http://argo.jcommops.org). The Argo Program is part of the Global Ocean Observing System. The marine mammal data were collected and made freely available by the International MEOP Consortium and the national programs that contribute to it (http://www.meop.net). The authors thank M. Vancoppenolle for very insightful discussions on sea-ice.

References

Barthélemy, A., T. Fichefet, H. Goosse, and G. Madec (2015), Modeling the interplay between sea ice formation and the oceanic mixed layer: Limitations of simple brine rejection parameterizations, *Ocean Modell.*, *86*, 141–152.
Barthélemy, A., T. Fichefet, and H. Goosse (2016), Spatial heterogeneity of ocean surface boundary conditions under sea ice, *Ocean Modell.*, *102*, 82–98.
Biuw, M., et al. (2007), Variations in behavior and condition of a Southern Ocean top predator in relation to in situ oceanographic conditions, *Proc. Natl. Acad. Sci. U. S. A.*, *104*(34), 13,705–13,710.
Brainerd, K. E., and M. C. Gregg (1995), Surface mixed and mixing layer depths, *Deep Sea Res., Part I*, *42*(9), 1521–1543.
Cavalieri, D. J., P. Gloersen, C. L. Parkinson, J. C. Comiso, and H. J. Zwally (1997), Observed hemispheric asymmetry in global sea ice changes, *Science*, *278*(5340), 1104–1106.
Charrassin, J.-B., et al. (2008), Southern Ocean frontal structure and sea-ice formation rates revealed by elephant seals, *Proc. Natl. Acad. Sci. U. S. A.*, *105*(33), 11,634–11,639.
Cisewski, B., V. H. Strass, and H. Prandke (2005), Upper-ocean vertical mixing in the antarctic polar front zone, *Deep Sea Res., Part II*, *52*(9), 1087–1108.
Close, S. E., and H. Goosse (2013), Entrainment-driven modulation of Southern Ocean mixed layer properties and sea ice variability in cmip5 models, *J. Geophys. Res. Oceans*, *118*, 2811–2827, doi:10.1002/jgrc.20226.
de Boyer Montégut, C., G. Madec, A. S. Fischer, A. Lazar, and D. Iudicone (2004), Mixed layer depth over the global ocean: An examination of profile data and a profile-based climatology, *J. Geophys. Res.*, *109*, C12003, doi:10.1029/2004JC002378.
de Lavergne, C., J. B. Palter, E. D. Galbraith, R. Bernardello, and I. Marinov (2014), Cessation of deep convection in the open Southern Ocean under anthropogenic climate change, *Nat. Clim. Change*, *4*(4), 278–282.
de Lavergne, C., G. Madec, J. Le Sommer, A. G. Nurser, and A. C. Naveira Garabato (2015), On the consumption of Antarctic bottom water in the abyssal ocean, *J. Phys. Oceanogr.*, *46*(2015), 635–661.
DeVries, T., and F. Primeau (2011), Dynamically and observationally constrained estimates of water-mass distributions and ages in the global ocean, *J. Phys. Oceanogr.*, *41*(12), 2381–2401.
Dong, S., S. T. Gille, and J. Sprintall (2007), An assessment of the Southern Ocean mixed layer heat budget, *J. Clim.*, *20*(17), 4425–4442.
Dong, S., J. Sprintall, S. T. Gille, and L. Talley (2008), Southern Ocean mixed-layer depth from Argo float profiles, *J. Geophys. Res.*, *113*, C06013, doi:10.1029/2006JC004051.
Dong, S., S. L. Garzoli, and M. Baringer (2009), An assessment of the seasonal mixed layer salinity budget in the Southern Ocean, *J. Geophys. Res.*, *114*, C12001, doi:10.1029/2008JC005258.
Fahrbach, E., M. Hoppema, G. Rohardt, M. Schröder, and A. Wisotzki (2004), Decadal-scale variations of water mass properties in the deep Weddell Sea, *Ocean Dyn.*, *54*(1), 77–91.
Gill, A. E. (1982), *Atmosphere-Ocean Dynamics*, vol. 30, Academic.
Goosse, H., and T. Fichefet (1999), Importance of ice-ocean interactions for the global ocean circulation: A model study, *J. Geophys. Res.*, *104*(C10), 23,337–23,355.
Gordon, A. L. (1991), Two stable modes of Southern Ocean winter stratification, *Elsevier Oceanogr. Ser.*, *57*, 17–35.
Gordon, A. L., and B. A. Huber (1990), Southern Ocean winter mixed layer, *J. Geophys. Res*, *95*(11), 655–611.
Gordon, A. L., M. Visbeck, and J. C. Comiso (2007), A possible link between the Weddell polynya and the southern annular mode*, *J. Clim.*, *20*(11), 2558–2571.
Haumann, F. A., N. Gruber, M. Münnich, I. Frenger, and S. Kern (2016), Sea-ice transport driving Southern Ocean salinity and its recent trends, *Nature*, *537*(7618), 89–92.
Holland, P. R., and R. Kwok (2012), Wind-driven trends in Antarctic sea-ice drift, *Nat. Geosci.*, *5*(12), 872–875.
Holte, J., and L. Talley (2009), A new algorithm for finding mixed layer depths with applications to Argo data and subantarctic mode water formation*, *J. Atmos. Oceanic Technol.*, *26*(9), 1920–1939.
IOC, SCOR, and IAPSO (2010), The international thermodynamic equation of seawater—2010: Calculation and use of thermodynamic properties, in *Intergovernmental Oceanographic Commission, Manuals and Guides*, vol. 56, 196 pp., UNESCO.
Iudicone, D., G. Madec, B. Blanke, and S. Speich (2008), The role of Southern Ocean surface forcings and mixing in the global conveyor, *J. Phys. Oceanogr.*, *38*(7), 1377–1400.
Johnson, G. C. (2008), Quantifying Antarctic bottom water and north Atlantic deep water volumes, *J. Geophys. Res.*, *113*, C05027, doi: 10.1029/2007JC004477.
Johnson, G. C., and S. C. Doney (2006), Recent western south Atlantic bottom water warming, *Geophys. Res. Lett.*, *33*, L14614, doi:10.1029/2006GL026769.
Karsten, R. H., and J. Marshall (2002), Constructing the residual circulation of the ACC from observations, *J. Phys. Oceanogr.*, *32*(12), 3315–3327.
Keeling, R. F., and M. Visbeck (2011), On the linkage between Antarctic surface water stratification and global deep-water temperature, *J. Clim.*, *24*(14), 3545–3557.
Lévy, M., O. Jahn, S. Dutkiewicz, M. J. Follows, and F. d'Ovidio (2015), The dynamical landscape of marine phytoplankton diversity, *J. R. Soc. Interface*, *12*(111), 20150481.
Lukas, R., and E. Lindstrom (1991), The mixed layer of the western equatorial Pacific Ocean, *J. Geophys. Res.*, *96*(S01), 3343–3357.
Lumpkin, R., and K. Speer (2007), Global ocean meridional overturning, *J. Phys. Oceanogr.*, *37*(10), 2550–2562.
Markus, T., C. Kottmeier, and E. Fahrbach (1998), *Ice Formation in Coastal Polynyas in the Weddell Sea and Their Impact on Oceanic Salinity*, vol. 74, pp. 273–292, John Wiley.
Marshall, J., D. Jamous, and J. Nilsson (1999), Reconciling thermodynamic and dynamic methods of computation of water-mass transformation rates, *Deep Sea Res., Part I*, *46*(4), 545–572.
Martinson, D. G., and R. A. Iannuzzi (1998), Antarctic ocean-ice interaction: Implications from ocean bulk property distributions in the Weddell gyre, *Antarct. Sea Ice*, *74*, 243–271.
Massom, R., P. Harris, K. J. Michael, and M. Potter (1998), The distribution and formative processes of latent-heat polynyas in east Antarctica, *Ann. Glaciol.*, *27*, 420–426.
Massom, R. A., and S. E. Stammerjohn (2010), Antarctic sea ice change and variability–physical and ecological implications, *Polar Sci.*, *4*(2), 149–186.
Mathiot, P., H. Goosse, T. Fichefet, B. Barnier, and H. Gallée (2011), Modelling the seasonal variability of the Antarctic slope current, *Ocean Sci.*, *7*(4), 445–532.

Orsi, A. H., T. Whitworth, and W. D. Nowlin (1995), On the meridional extent and fronts of the Antarctic circumpolar current, *Deep Sea Res., Part I*, *42*(5), 641–673.
Orsi, A. H., S. S. Jacobs, A. L. Gordon, and M. Visbeck (2001), Cooling and ventilating the abyssal ocean, *Geophys. Res. Lett.*, *28*(15), 2923–2926.
Petty, A., P. Holland, and D. Feltham (2014), Sea ice and the ocean mixed layer over the Antarctic shelf seas, *Cryosphere*, *7*(4), 4321–4377.
Reeve, K., O. Boebel, T. Kanzow, V. Strass, G. Rohardt, and E. Fahrbach (2015), Objective mapping of argo data in the Weddell gyre: A gridded dataset of upper ocean water properties, *Earth Syst. Sci. Data Discuss.*, *8*(1), 509–566.
Ren, L., and S. C. Riser (2009), Seasonal salt budget in the northeast Pacific Ocean, *J. Geophys. Res.*, *114*, C12004, doi:10.1029/2009JC005307.
Ren, L., K. Speer, and E. P. Chassignet (2011), The mixed layer salinity budget and sea ice in the Southern Ocean, *J. Geophys. Res.*, *116*, C08031, doi:10.1029/2010JC006634.
Rintoul, S. R., J. Church, E. Fahrbach, M. Garcia, A. Gordon, B. King, R. Morrow, A. Orsi, and K. Speer (2001), Monitoring and understanding Southern Ocean variability and its impact on climate: A strategy for sustained observations, in *Observing the Ocean for Climate in the 21st Century*, edited by C. Koblinsky and N. Smith, GODAE Project Off., Bur. of Meteorol., Melbourne, Victoria, Australia.
Rio, M.-H., S. Mulet, and N. Picot (2014), Beyond GOCE for the ocean circulation estimate: Synergetic use of altimetry, gravimetry, and in situ data provides new insight into geostrophic and Ekman currents, *Geophys. Res. Lett.*, *41*, 8918–8925, doi:10.1002/2014GL061773.
Riser, S. C., et al. (2016), Fifteen years of ocean observations with the global Argo array, *Nat. Clim. Change*, *6*(2), 145–153.
Roquet, F., et al. (2013), Estimates of the southern ocean general circulation improved by animal-borne instruments, *Geophys. Res. Lett.*, *40*, 6176–6180, doi:10.1002/2013GL058304.
Roquet, F., et al. (2014), A southern Indian ocean database of hydrographic profiles obtained with instrumented elephant seals, *Sci. data*, *1*, 140028.
Roquet, F., G. Madec, T. J. McDougall, and P. M. Barker (2015), Accurate polynomial expressions for the density and specific volume of seawater using the teos-10 standard, *Ocean Modell.*, *90*, 29–43.
Sallée, J.-B., N. Wienders, K. Speer, and R. Morrow (2006), Formation of subantarctic mode water in the southeastern Indian ocean, *Ocean Dyn.*, *56*(5-6), 525–542.
Sallée, J.-B., R. Morrow, and K. Speer (2008), Eddy heat diffusion and subantarctic mode water formation, *Geophys. Res. Lett.*, *35*, L05607, doi:10.1029/2007GL032827.
Sallée, J.-B., K. Speer, S. Rintoul, and S. Wijffels (2010), Southern Ocean thermocline ventilation, *J. Phys. Oceanogr.*, *40*(3), 509–529.
Sallée, J.-B., R. J. Matear, S. R. Rintoul, and A. Lenton (2012), Localized subduction of anthropogenic carbon dioxide in the southern hemisphere oceans, *Nat. Geosci.*, *5*(8), 579–584.
Schmidtko, S., G. C. Johnson, and J. M. Lyman (2013), @@MIMOC: A global monthly isopycnal upper-ocean climatology with mixed layers, *J. Geophys. Res. Oceans*, *118*, 1658–1672, doi:10.1002/jgrc.20122.
Sigman, D. M., and E. A. Boyle (2000), Glacial/interglacial variations in atmospheric carbon dioxide, *Nature*, *407*(6806), 859–869.
Sigman, D. M., M. P. Hain, and G. H. Haug (2010), The polar ocean and glacial cycles in atmospheric CO_2 concentration, *Nature*, *466*(7302), 47–55.
Sprintall, J., and D. Roemmich (1999), Characterizing the structure of the surface layer in the Pacific Ocean, *J. Geophys. Res.*, *104*(C10), 23,297–23,311.
Talley, L. D., M. D. Sparrow, P. Chapman, and J. Gould (2007), *Hydrographic Atlas of the World Ocean Circulation Experiment (WOCE). Volume 2: Pacific Ocean*, edited by M. Sparrow et al., WOCE Int. Project Off., Southampton, U. K.
Tamura, T., K. I. Ohshima, and S. Nihashi (2008), Mapping of sea ice production for Antarctic coastal polynyas, *Geophys. Res. Lett.*, *35*, L07606, doi:10.1029/2007GL032903.
Tamura, T., K. I. Ohshima, S. Nihashi, and H. Hasumi (2011), Estimation of surface heat/salt fluxes associated with sea ice growth/melt in the Southern Ocean, *SOLA*, *7*, 17–20.
Thomson, R. E., and I. V. Fine (2003), Estimating mixed layer depth from oceanic profile data, *J. Atmos. Oceanic Technol.*, *20*(2), 319–329.
Thorndike, A., and R. Colony (1982), Sea ice motion in response to geostrophic winds, *J. Geophys. Res.*, *87*(C8), 5845–5852.
Vancoppenolle, M., T. Fichefet, H. Goosse, S. Bouillon, G. Madec, and M. A. M. Maqueda (2009), Simulating the mass balance and salinity of arctic and Antarctic sea ice. 1. Model description and validation, *Ocean Modell.*, *27*(1), 33–53.
Whitworth, T., A. Orsi, S.-J. Kim, W. Nowlin, and R. Locarnini (1998), Water masses and mixing near the Antarctic slope front, in *Ocean, Ice, and Atmosphere: Interactions at the Antarctic Continental Margin*, pp. 1–27.
Wu, L., Z. Jing, S. Riser, and M. Visbeck (2011), Seasonal and spatial variations of Southern Ocean diapycnal mixing from Argo profiling floats, *Nat. Geosci.*, *4*(6), 363–366.
You, Y. (2002), A global ocean climatological atlas of the turner angle: Implications for double-diffusion and water-mass structure, *Deep Sea Res., Part I*, *49*(11), 2075–2093.
Zhang, J. (2007), Increasing Antarctic sea ice under warming atmospheric and oceanic conditions, *J. Clim.*, *20*(11), 2515–2529.
Zwally, H. J., J. C. Comiso, C. L. Parkinson, D. J. Cavalieri, and P. Gloersen (2002), Variability of Antarctic sea ice 1979–1998, *J. Geophys. Res.*, *107*(C5), 3041, doi:10.1029/2000JC000733.